MOM ANALYSIS OF CONDUCTING STRUCTURES INVOLVING BOTH SURFACES AND WIRES BY USING JUNCTION BASIS FUNCTIONS

A THESIS SUBMITTED TO
THE GRADUATE SCHOOL OF NATURAL AND APPLIED SCIENCES
OF
MIDDLE EAST TECHNICAL UNIVERSITY

BY

KUTLUHAN DEMİRCAN

IN PARTIAL FULFILLMENT OF THE REQUIREMENTS
FOR
THE DEGREE OF MASTER OF SCIENCE
IN
ELECTRICAL AND ELECTRONICS ENGINEERING

FEBRUARY 2015

Approval of the thesis:

MOM ANALYSIS OF CONDUCTING STRUCTURES INVOLVING BOTH SURFACES AND WIRES BY USING JUNCTION BASIS FUNCTIONS

submitted by **KUTLUHAN DEMİRCAN** in partial fulfillment of the requirements for the degree of **Master of Science in Electrical & Electronics Engineering Department, Middle East Technical University** by,

Prof. Dr. Gülbin DURAL
Dean, Graduate School of **Natural and Applied Sciences**

Prof. Dr. Gönül TURHAN SAYAN
Head of Department, **Electrical and Electronics Engineering**

Assoc. Prof. Dr. Lale ALATAN
Supervisor, **Electrical and Electronics Engineering Dept., METU**

Examining Committee Members:

Prof. Dr. Gülbin DURAL
Electrical and Electronics Engineering Dept., METU

Assoc. Prof. Dr. Lale ALATAN
Supervisor, Electrical and Electronics Engineering Dept., METU

Prof. Dr. Özlem AYDIN ÇİVİ
Electrical and Electronics Engineering Dept., METU

Prof. Dr. Mustafa KUZUOĞLU
Electrical and Electronics Engineering Dept., METU

Assoc. Prof. Dr. Vakur Behçet ERTÜRK
Electrical and Electronics Engineering Dept., Bilkent University

Date: 13.02.2015

I hereby declare that all information in this document has been obtained and presented in accordance with academic rules and ethical conduct. I also declare that, as required by these rules and conduct, I have fully cited and referenced all material and results that are not original to this work.

Name, Last name : Kutluhan DEMİRCAN

Signature :

ABSTRACT

MOM ANALYSIS OF CONDUCTING STRUCTURES INVOLVING BOTH SURFACES AND WIRES BY USING JUNCTION BASIS FUNCTIONS

Demircan, Kutluhan
M.Sc., Electrical and Electronics Engineering Department
Supervisor : Assoc. Prof. Dr. Lale Alatan
February 2015, 63 pages

In this thesis a structure with thin wire attached to a PEC plate is analyzed numerically by using Method of Moments (MoM) with Galerkin's testing scheme. The structure is divided into two parts: the plate and the thin wire and each part is analyzed separately. The RWG basis functions are chosen as basis/testing functions for the plate, piecewise linear basis/testing function is chosen for the thin wire and an attachment mode basis function that is compatible with RWG and piecewise linear basis functions is applied at the junction. To overcome the singularity problem that occurs during the computation of MoM matrix entries, different singularity handling methods are used and the obtained results are presented. First, scattering from a conducting plate and a conducting wire are analyzed separately. Then these two structures are combined in a non-contacting configuration and this combined structure is analyzed by incorporating the interaction between the wire and the plate. Finally, these two structures are combined in a contacting configuration and analyzed by making use of an attachment current at the contact point.

Keywords: Method of Moments, RWG, attachment mode, junction mode

ÖZ

İLETKEN LEVHA VE TEL İÇEREN YAPILARIN BİRLEŞME YERİ TEMEL FONKSİYONLARI KULLANARAK MOMENTLER YÖNTEMİYLE ANALİZİ

Demircan, Kutluhan
Yüksek Lisans, Elektrik ve Elektronik Mühendisliği Bölümü
Tez Yöneticisi : Doç. Dr. Lale Alatan
Şubat 2015, 63 sayfa

Bu yüksek lisans tez çalışmasında, bir iletken telin bir iletken levha ile birleşiminden oluşan yapıdaki akım dağılımının momentler metodu kullanılarak Galerkin test yöntemi ile analiz edilmiştir. Bu yapı, iletken levha ve tel olmak üzere 2 kısımda incelenmiştir ve her kısım ayrı ayrı analiz edilmiştir. Levhanın analizi için temel ve test fonksiyonu olarak RWG temel fonksiyonları, telin analizi için üçgen temel/test fonksiyonu, bağlantı noktası için ise RWG ve üçgen temel fonksiyonlar ile uyumlu olan bir temel fonksiyon kullanılmıştır. Momentler metodu matris değerleri hesaplanırken ortaya çıkan tekillikler, farklı yönetme metotları ile çözümlenmiştir ve elde edilen sonuçlar sergilenmiştir. İlk olarak, iletken levhadan ve telden saçınım ayrı ayrı analiz edilmiştir. Sonrasında bu iki yapı birleştirilerek, temas etmeyen bir konfigürasyonda, levha ile telin etkileşimi de eklenerek analiz edilmiştir. Son olarak, bu levha ve tel temas eden bir konfigürasyonda birleştirilerek, bağlantı noktasındaki akım dağılımı da eklenerek analiz edilmiştir.

Anahtar Kelimeler: Momentler metodu, RWG, birleşim noktası

To my beloved wife and my dear parents.

ACKNOWLEDGEMENTS

The author wishes to express his deepest gratitude to his supervisor Assoc. Prof. Dr. Lale Alatan for her guidance, advice, encouragements and patience throughout the research.

The author would also like to thank his friend Adil Fırat Yılmaz for his supports.

TABLE OF CONTENTS

CHAPTERS

LIST OF FIGURES

CHAPTER 1

INTRODUCTION

In the design and analysis of systems working at microwave frequencies, computational electromagnetics plays a very important role. Computational electromagnetics refers to the numerical solution of Maxwell’s equation together with boundary conditions specified by the shape, size and materials of the structure under consideration. The simulation results obtained from computational methods not only make the solution of complex systems possible but also help to visualize the behavior of the system under certain conditions and environment.

Among several analysis methods in computational electromagnetics, the Method of Moments (MoM) [1] is known to be the best analysis method for radiation and scattering problems, because it requires only the discretization of surface currents on conductors and volume currents in dielectric materials, rather than values throughout the space. Moreover the radiation condition is considered in the formulation of the Green’s function, therefore no extra effort is required to handle open geometries that radiate to unbounded medium.

Not only in military but also in commercial communication and radar systems, more and more intelligent and complex antenna structures are used. Even the cars that are used in everyday life are now equipped with smart antenna systems for full automated parking. Most of the complex antenna structures for such applications are composed of both conducting surfaces and wires. In the MoM analysis of such antennas the basis functions used to model the surfaces and wires are quite different, and additional basis functions need to be utilized at the intersection of surfaces and wires to account for the continuity of the current at the junction.

In this thesis work, a MoM based simulation software is developed to analyze structures that involve both conducting surfaces and wires. RWG (Rao-Wilton-Glisson) [2] basis functions are used for conducting surfaces and piecewise linear (triangle) basis functions are employed for wires. Junction basis functions [3], [4],

[5] that conform to RWG basis functions on the surface and triangles on the wire are utilized at the intersection of surfaces with wires.

In the application of MoM, a singularity problem arises when the basis and testing functions coincide during the computation of self terms. To handle the singularity problem associated with the analysis of surfaces, two different approaches proposed in [6] and [7] are utilized and the results are compared.

The singularity problem encountered in the analysis of the thin wires is eliminated by making use of the approach proposed in [8].

To verify the software developed within the scope of this thesis, the current distribution on a PEC square plate with a thin wire attached to it will be analyzed. In order to reduce the overall complexity of the problem, the problem is partitioned into several sections:

1- Obtaining the surface currents on a PEC square plate using structured triangular mesh under the excitation of a plane wave.
2- Obtaining the current distribution on a thin wire dipole antenna under delta-gap excitation.
3- Combining a thin wire and PEC square plate in a non-contacting configuration and obtaining the current distribution on the vertical dipole/monopole and surface currents on the PEC plate.
4- Combining a thin wire and PEC square plate in a contacting configuration and obtaining the surface currents on the overall system by using the attachment mode.

The organization of the thesis is as follows:

In the second chapter, the derivation of the electric field integral equation (EFIE) and its solution by using the Method of Moments (MoM) is reviewed.

Chapter 3 contains the MoM analysis of conducting surfaces. Two different methods which are used to handle singular integrals involved in the evaluation of the MoM matrix entries are discussed. The results obtained for a PEC plate are presented and compared.

Chapter 4 contains the MoM analysis of wires, including the approach used to overcome the singularity problem. The simulation results obtained for dipole antennas are presented.

Chapter 5 contains the MoM analysis of non-contacting surface-wire couplings. As a demonstrative example a dipole over a PEC plate is analyzed and the simulation results of the developed code is compared with simulation results obtained from commercially available software FeKo.

Chapter 6 contains the MoM formulation of surfaces and wires connected to each other. Junction basis function (attachment mode) is defined to model the current at the intersection of wire and surface. The results for a top-loaded monopole antenna are presented and compared with the results found in literature.

Chapter 7 contains the conclusion and future work.

CHAPTER 2

METHOD OF MOMENTS SOLUTION OF ELECTRIC FIELD INTEGRAL EQUATION

2.1 MAXWELL’S EQUATIONS

Maxwell’s equations define the relationships between electric and magnetic fields and how they are generated by each other. The equations for a homogenous medium with permittivity ε and permeability μ are:

$$\nabla \times \boldsymbol{E} = -\boldsymbol{M} - j\omega\mu\boldsymbol{H} \tag{2.1}$$

$$\nabla \times \boldsymbol{H} = \boldsymbol{J} + j\omega\varepsilon\boldsymbol{E} \tag{2.2}$$

$$\nabla \cdot \boldsymbol{D} = q_e \tag{2.3}$$

$$\nabla \cdot \boldsymbol{B} = q_m \tag{2.4}$$

To be able to apply Maxwell’s equations, the relationships between displacement field **D** and electric field intensity **E**, as well as the magnetic flux **B** and magnetic field intensity **H** must be defined. **T**he constitutive relations define these relations:

$$\boldsymbol{D} = \varepsilon\boldsymbol{E} \tag{2.5}$$

$$\boldsymbol{B} = \mu\boldsymbol{H}. \tag{2.6}$$

2.2 ELECTROMAGNETIC BOUNDARY CONDITIONS

At the interfaces of two different materials, a discontinuity may occur in the fields. To be able to apply Maxwell’s equations to discontinuous fields, some boundary conditions must be defined. These boundary conditions are obtained using the integral form of the Maxwell’s equations.

The figure below shows a representation of a medium interface, where $\hat{\boldsymbol{n}}$ shows the surface normal and $\hat{\boldsymbol{t}}$ shows the tangential vector.

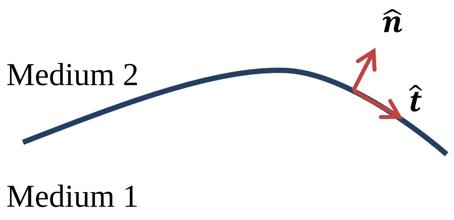

Figure 1 - A representation of a medium interface

The general form of the boundary conditions is as below:

$$-\hat{\boldsymbol{n}} \times (\boldsymbol{E_2} - \boldsymbol{E_1}) = \boldsymbol{M_s} \tag{2.7}$$

$$\hat{\boldsymbol{n}} \times (\boldsymbol{H_2} - \boldsymbol{H_1}) = \boldsymbol{J_s} \tag{2.8}$$

$$\hat{\boldsymbol{n}} \cdot (\boldsymbol{D_2} - \boldsymbol{D_1}) = \boldsymbol{q_e} \tag{2.9}$$

$$\hat{\boldsymbol{n}} \cdot (\boldsymbol{B_2} - \boldsymbol{B_1}) = \boldsymbol{q_m} \tag{2.10}$$

where, $\boldsymbol{J_s}$ and $\boldsymbol{M_s}$ are surface electric and magnetic current densities and $\boldsymbol{q_e}$ and $\boldsymbol{q_m}$ are surface electric and magnetic charge densities, respectively.

The boundary conditions can be simplified for a PEC object (assuming medium 1).

$$-\hat{\boldsymbol{n}} \times \boldsymbol{E_2} = \boldsymbol{0} \tag{2.11}$$

$$\hat{\boldsymbol{n}} \times \boldsymbol{H_2} = \boldsymbol{J_s} \tag{2.12}$$

$$\hat{\boldsymbol{n}} \cdot \boldsymbol{D_2} = \boldsymbol{q_e} \tag{2.13}$$

$$\hat{\boldsymbol{n}} \cdot \boldsymbol{B_2} = \boldsymbol{0} \tag{2.14}$$

2.3 ELECTRIC FIELD INTEGRAL EQUATION (EFIE)

In the analysis of scattering from PEC objects, either an electric field integral equation (EFIE) or a magnetic field integral equation (MFIE) can be obtained by imposing the boundary conditions given in (2.11) and (2.12), respectively. In this thesis, EFIE is chosen and it is derived by using vector ($\boldsymbol{A}$) and scalar (ϕ) potentials.

An incident electric field $\boldsymbol{E^i}(\boldsymbol{r})$ induces a surface current on the object, which in return causes to a scattered field $\boldsymbol{E^s}(\boldsymbol{r})$. According to the equivalence theorem, the sum of these fields defines the total field. Applying the boundary conditions for the

PEC object from equation (2.11), the sum of the tangential components of these fields result in:

$$\hat{\boldsymbol{n}} \times \boldsymbol{E}^{s}(\boldsymbol{r}) = -\hat{\boldsymbol{n}} \times \boldsymbol{E}^{i}(\boldsymbol{r}) \qquad (2.15)$$

The relation between surface current density $\boldsymbol{J}$ and scattered field can be obtained by using the equation (2.16)

$$\boldsymbol{E}^{s}(\boldsymbol{r}) = -j\omega \boldsymbol{A}(\boldsymbol{r}) - \nabla\phi(\boldsymbol{r}) \qquad (2.16)$$

where, $\boldsymbol{A}$ and ϕ can be expressed in terms of free space scalar Green's function as:

$$\boldsymbol{A}(\boldsymbol{r}) = \frac{\mu}{4\pi}\int_S \boldsymbol{J}\frac{e^{-jk|r-r'|}}{|\boldsymbol{r}-\boldsymbol{r}'|}dS' \qquad (2.17)$$

$$\phi(\boldsymbol{r}) = \frac{1}{4\pi\varepsilon}\int_S \rho\frac{e^{-jk|r-r'|}}{|\boldsymbol{r}-\boldsymbol{r}'|}dS' \qquad (2.18)$$

$$\rho = \frac{\nabla\cdot\boldsymbol{J}}{-j\omega} \qquad (2.19)$$

By substituting (2.17) through (2.19) into (2.16), (2.15) can be written as:

$$\hat{\boldsymbol{n}} \times \boldsymbol{E}^{i}(\boldsymbol{r}) = \hat{\boldsymbol{n}} \times \left[j\omega\mu \begin{pmatrix} \int_S \boldsymbol{J}(\boldsymbol{r})G(\boldsymbol{r},\boldsymbol{r}')dS' + \\ \int_S \nabla(\nabla\cdot\boldsymbol{J}(\boldsymbol{r}))G(\boldsymbol{r},\boldsymbol{r}')dS' \end{pmatrix} \right] \qquad (2.20)$$

Here, $G(\boldsymbol{r},\boldsymbol{r}')$ represents the free space scalar Green's function, which describes a spherical wave propagating away from point $\boldsymbol{r}'$.

$$G(\boldsymbol{r},\boldsymbol{r}') = \frac{e^{-jk|r-r'|}}{4\pi|\boldsymbol{r}-\boldsymbol{r}'|} \qquad (2.21)$$

The EFIE is a Fredholm integral equation of the first kind, where the current appears inside the integral sign only. Because the derivation did not impose any constraint on the shape of the scatterer, the EFIE may be applied to closed surfaces as well as open, thin objects. For thin surfaces, the current represents the vector sum of the current density on both sides of the scatterer [9].

The EFIE is not possible to be solved analytically except for some canonical problems. Therefore, these equations must be solved using computational methods that are to be configured specifically for the problem of interest.

In the following section one of the computational analysis methods; the Method of Moment (MoM) is introduced. Using MoM, these integral equations can be converted to a system of linear equations that can be solved numerically using linear algebra methods.

2.4 THE METHOD OF MOMENTS

The MoM formulation will be presented for a general operator equation defined as:

$$\mathcal{L}\big(f(x)\big) = g(x) \tag{2.22}$$

where $\mathcal{L}$ is a linear operator, g is a known function and f is the unknown function. In our problem, $g(x)$is the incident electric field and $f(x)$ is the current induced on the PEC surface. $f(x)$ can be expanded in terms of known basis functions.

$$f(x) = \sum_{n=1}^{N} a_n f_n(x) \tag{2.23}$$

Here, $f_n(x)$ denotes the basis functions and a_n denote the unknown coefficients (weights). The basis functions are chosen to model the expected behavior of the unknown function throughout its domain, and can be scalars or vectors depending on the problem. If the basis functions have local support in the domain, they are called local or subsectional basis functions. If their support spans the entire problem domain, they are called global or entire-domain basis functions [9].

Since, the operator $\mathcal{L}$ is linear, $\mathcal{L}(f(x))$ can be written as:

$$\mathcal{L}(f(x)) = \sum_{n=1}^{N} a_n \, \mathcal{L}(f_n(x)) \approx g(x) \tag{2.24}$$

And the residual R can be defined as:

$$\mathrm{R} = g(x) - \sum_{n=1}^{N} a_n \, \mathcal{L}(f_n(x)) \tag{2.25}$$

The aim is to make the residual equal to zero, but it is a function of x. Therefore, it can be equated to zero in the average sense by defining an inner product integral between functions f and w:

$$< w, f > = \int_{\Omega} wf \, d\Omega \tag{2.26}$$

By defining a set of testing (or weighting) functions w_m, the weighted residual is equated to zero as:

$$\sum_{n=1}^{N} a_n < \boldsymbol{w}_m, \mathcal{L}(\boldsymbol{f}_n(x)) > = < \boldsymbol{w}_m, \boldsymbol{g}(x) > \qquad (2.27)$$

The equation (2.41) results in a set of linear equations in the form $\boldsymbol{Za} = \boldsymbol{b}$ with the following elements.

$$Z_{mn} =< \boldsymbol{w}_m, \mathcal{L}(\boldsymbol{f}_n) > \qquad (2.28)$$

$$b_m =< \boldsymbol{w}_m, \boldsymbol{g} > \qquad (2.29)$$

Note that the number of weighting functions; M, should be chosen to be equal to the number of unknowns; N. The unknown coefficients (entries of a vector) can be easily calculated by solving the matrix equation $\boldsymbol{Za} = \boldsymbol{b}$.

Different sets of testing functions results in different matrix equation. When same set of functions are used as basis and testing, the method is called as Galerkin’s method. Since Galerkin’s testing scheme results in symmetrical matrices, this method is preferred in this thesis to reduce the computation time by exploiting symmetry.

For our problem as stated before, the surface current density induced on the PEC is our unknown function. The surface current $\boldsymbol{J}$ can be expressed as a sum of basis functions:

$$\boldsymbol{J} = \sum_{n=1}^{N} a_n \boldsymbol{f}_n \qquad (2.30)$$

Then, the elements of the impedance matrix $\boldsymbol{Z}$ can be rewritten from (2.28) for this problem as:

$$Z_{mn} =< \boldsymbol{w}_m, \mathcal{L}(\boldsymbol{f}_n) >= \int_{\Omega_m} \boldsymbol{w}_m \cdot \mathcal{L}(\boldsymbol{f}_n)\, d\Omega \qquad (2.31)$$

$\mathcal{L}(\boldsymbol{f}_n)$ can be interpreted as the electric field due to the source current $\boldsymbol{f}_n$, so this integral will be referred as source integral in the rest of this thesis. Whereas, the integral in $< \boldsymbol{w}_m, \mathcal{L}(\boldsymbol{f}_n) >$ corresponds to the testing of this electric field at the observation points within the domain of $\boldsymbol{w}_m$.

The excitation matrix $\boldsymbol{b}$ can be written for our problem as:

$$b_m =< \boldsymbol{w}_m, \boldsymbol{E^i} >= \int_{\Omega_m} \boldsymbol{w}_m \cdot \boldsymbol{E^i}\, d\Omega \qquad (2.32)$$

In the following chapters, the explicit expressions for Z_{mn} and b_m will be presented for the corresponding choice of basis functions.

CHAPTER 3

MoM ANALYSIS OF SURFACES

Solving the electric field integral equation (EFIE) for a body requires a mesh and an appropriate basis function to the geometry. In the last years, the triangular mesh is proven to be the best mesh type to represent structures. The RWG (Rao-Wilton-Glisson) basis functions, which define surface currents on triangular patches, result in the most reliable solution for triangular meshed structures.

3.1 RWG BASIS FUNCTIONS

The RWG basis functions [2] consist of a pair of triangles that share an edge. This common edge is to be an interior edge in the mesh. Therefore, in a triangular meshed structure, it can be said that every interior edge defines an RWG basis function.

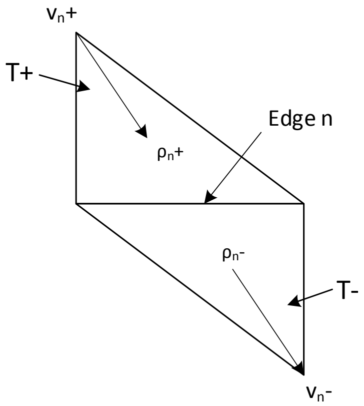

Figure 2 - RWG basis function [9]

Here, the vectors $\boldsymbol{\rho_n^-}$ and $\boldsymbol{\rho_n^+}$ show the direction components of the surface current. In this notation, $\boldsymbol{\rho_n^+}$ is pointed away from the vertex $\boldsymbol{v_n^+}$ and $\boldsymbol{\rho_n^-}$ is pointed towards $\boldsymbol{v_n^-}$. Therefore, the vectors $\boldsymbol{\rho_n^-}$ and $\boldsymbol{\rho_n^+}$ can be written as:

$$\boldsymbol{\rho}_n^- = \boldsymbol{v}_n^- - \boldsymbol{r} \tag{3.1}$$

$$\boldsymbol{\rho}_n^+ = \boldsymbol{r} - \boldsymbol{v}_n^+ \tag{3.2}$$

Lastly, T_n^- and T_n^+ refer to the (-) and (+) triangles of the RWG basis function. Using this notation, the basis functions are defined as:

$$\boldsymbol{f}_n(\boldsymbol{r}) = \begin{cases} \frac{l_n}{2A_n^+}\boldsymbol{\rho}_n^+, \ \boldsymbol{r} \ in \ T_n^+ \\ \frac{l_n}{2A_n^-}\boldsymbol{\rho}_n^-, \ \boldsymbol{r} \ in \ T_n^- \\ 0, \ otherwise \end{cases} \tag{3.3}$$

Here, l_n refers to the length of the edge, A_n^+ and A_n^- refer to the area of the triangular patches T_n^+ and T_n^-, respectively.

In order to use this basis function in the EFIE formulation, also the divergence of the basis function $\boldsymbol{f}_n(\boldsymbol{r})$ is required, which is:

$$\nabla_s \cdot \boldsymbol{f}_n(\boldsymbol{r}) = \begin{cases} \frac{l_n}{A_n^+}, \ \boldsymbol{r} \ in \ T_n^+ \\ -\frac{l_n}{A_n^-}, \ \boldsymbol{r} \ in \ T_n^- \\ 0, otherwise \end{cases} \tag{3.4}$$

3.2 MESH GENERATION FOR THE PLATE

In order to analyze the PEC square plate, a structured triangular mesh is defined and generated. The structured mesh shown in Figure 3 is chosen for the problem analysis. In order to generate this mesh structure an algorithm is developed and implemented as a MatLab function.

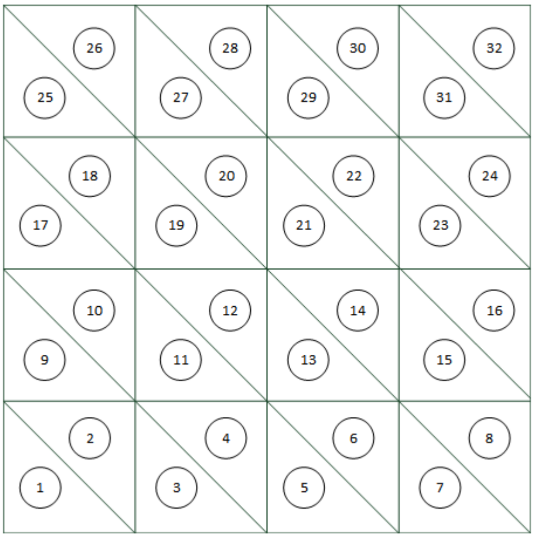

Figure 3 - Mesh structure

In Figure 3, the numbering for the triangles for a mesh with 32 triangles can be seen. For the mesh generation, the lengths of the plate in x-axis, y-axis and the step size are taken as input and a virtual coordinate system is generated with numbering the triangles, identifying crucial coordinate points and the RWG elements.

The first output of the mesh generation is an array that contains the triangle numbers of each RWG pairs. For example, one of the RWG pairs consists of the triangle #1 and triangle #2.

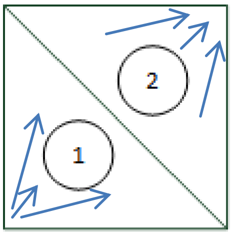

Figure 4 - Triangle numbers

The second output of the mesh generation is an array that contains all vertex coordinates of the triangles in (x_1,y_1,z_1,x_2,y_2,z_2,x_3,y_3,z_3) format. In the chosen mesh structure, there are two types of triangles: lower triangle (LT) and upper triangle (UT). The order of the vertex coordinates for each triangle is shown in Figure 5:

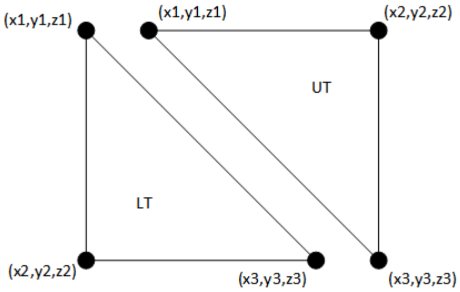

Figure 5 - Vertices of triangles

The third output is the area of a triangle. Since a structured mesh is used, all triangles have the same area.

The last output is the number that denotes the type of RWG pair. Since, each interior edge in the mesh defines an RWG pair, it is important to identify the interior edges in the generated mesh and to identify the RWG pairs. In the selected mesh structure there are basically 3 types of interior edges as shown in Figure 6.

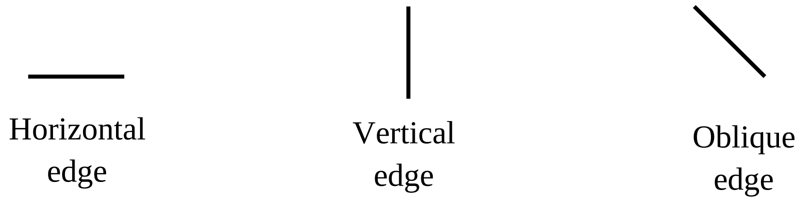

Figure 6 - Edge types

Each type of interior edges, defines a different type of RWG pair as shown in Figure 7.

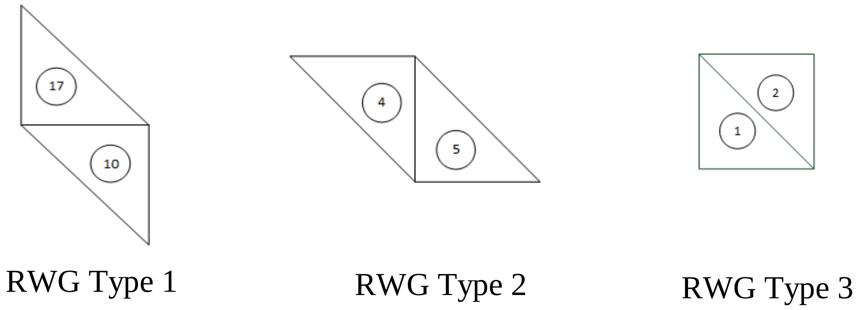

Figure 7 - RWG types

During the mesh generation, each of these RWG types are identified in the mesh and the amount of each type is saved in an array.

Another important information about the triangles is the coordinates of the Gaussian quadrature points. Because computation of MoM matrix entries requires the evaluation of integrals on the triangular surfaces, the calculation of these integrals need to be employed numerically. One of the approaches, for numerical integration over a triangular domain is the Gaussian quadrature rule [10]. In Gauss quadrature method, the integral is transformed into a weighted summation over a certain number of data points. The coordinates of these data points and their corresponding weighting coefficients can be obtained from tabulated values. These tabulated values for a standard unit triangle are shown in Figure 8.

In [10], it is suggested that when the integral domain is a standard unit triangle, the integral of a function over a triangular domain can be approximated as:

$$\int_A f(\alpha,\beta)dA = \frac{1}{2}\sum_{i=1}^{3} w_i f(\alpha_i,\beta_i) \qquad (3.5)$$

where, w_i is the weight and α_i, β_i is the coordinates of the i-th Gaussian quadrature point.

For Gaussian quadrature of degree 1, Gauss quadrature point is the centroid of the triangle and the values for w, α, β are:

$$(\alpha_1, \beta_1) = \left(\frac{1}{3}, \frac{1}{3}\right) \ with \ w_1 = 1 \tag{3.6}$$

For Gaussian quadrature of degree 2, Gauss quadrature points are shown in Figure 8 and the values for w, α, β, γ are:

$$(\alpha_1, \beta_1) = \left(\frac{2}{3}, \frac{1}{6}\right) \ with \ w_1 = \frac{1}{3} \tag{3.7}$$

$$(\alpha_2, \beta_2) = \left(\frac{1}{6}, \frac{2}{3}\right) \ with \ w_2 = \frac{1}{3} \tag{3.8}$$

$$(\alpha_3, \beta_3) = \left(\frac{1}{6}, \frac{1}{6}\right) \ with \ w_3 = \frac{1}{3} \tag{3.9}$$

The corresponding quadrature points on the standard unit triangle are shown in Figure 8.

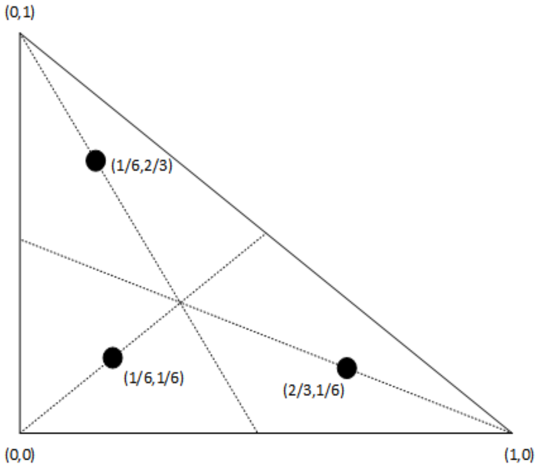

Figure 8 - Gaussian quadrate points for standard unit triangle

Since the mesh triangles are not standard unit triangles as in Figure 8, the calculation points $\boldsymbol{r}'$on the source triangles in the mesh structure must be transformed into the standard unit triangles. A source triangle described by vertex vectors $\boldsymbol{v}_1, \boldsymbol{v}_2, \boldsymbol{v}_3$is shown in Figure 9.

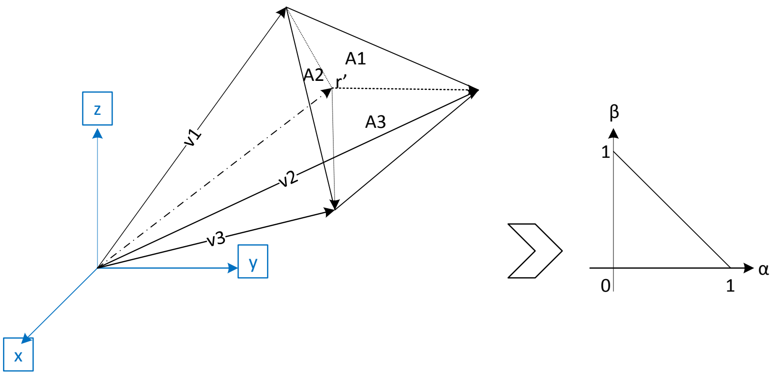

Figure 9 - Triangle transformation for Gaussian quadrature

Any interior point $\boldsymbol{r}'$ on the source triangle can be written in terms of vertex vectors and α, β as:

$$\boldsymbol{r}' = \alpha \boldsymbol{v}_1 + \beta \boldsymbol{v}_2 + (1 - \alpha - \beta)\boldsymbol{v}_3 \qquad (3.10)$$

For the integration, using Gaussian quadrature of degree 1, the following $\boldsymbol{r}'$ value must be used:

$$\boldsymbol{r}' = \frac{1}{3}\boldsymbol{v}_1 + \frac{1}{3}\boldsymbol{v}_2 + \frac{1}{3}\boldsymbol{v}_3 \qquad (3.11)$$

For the integration, using Gaussian quadrature of degree 2, the following 3 $\boldsymbol{r}'$ values must be used:

$$\boldsymbol{r}'_1 = \frac{2}{3}\boldsymbol{v}_1 + \frac{1}{6}\boldsymbol{v}_2 + \frac{1}{6}\boldsymbol{v}_3 \qquad (3.12)$$

$$\boldsymbol{r}'_2 = \frac{1}{6}\boldsymbol{v}_1 + \frac{2}{3}\boldsymbol{v}_2 + \frac{1}{6}\boldsymbol{v}_3 \qquad (3.13)$$

$$\boldsymbol{r}'_3 = \frac{1}{6}\boldsymbol{v}_1 + \frac{1}{6}\boldsymbol{v}_2 + \frac{2}{3}\boldsymbol{v}_3 \qquad (3.14)$$

So, for the numerical integration over a triangle in the generated mesh, $\boldsymbol{r}'$ must be replaced by these values. After this transformation, the weighted summation in (3.5) is computed and the result is multiplied by two times the area of the source triangle to account for the Jacobian of the transformation.

3.3 METHOD OF MOMENTS FORMULATION

Once the mesh information is obtained for the PEC plate, the Method of Moments analysis can be done. For this, as described in the Chapter 2, the problem must be transformed into the following form:

$$\boldsymbol{Za} = \boldsymbol{b} \tag{3.15}$$

Recall that a MoM matrix entry (Z_{mn}) was the testing of the electric field due to the source current $\boldsymbol{f}_n$ with the testing function $\boldsymbol{w}_m$. A matrix entry can be expressed in terms of vector and scalar potentials as:

$$Z_{mn} = j\omega < \boldsymbol{w}_m, \boldsymbol{A}(\boldsymbol{r}) > + < \boldsymbol{w}_m, \boldsymbol{\nabla}\phi(\boldsymbol{r}) > \tag{3.16}$$

When RWG testing functions are used, the first term of (3.16) is decomposed into two parts corresponding to positive and negative triangles as:

$$< \boldsymbol{w}_m, \boldsymbol{A}(\boldsymbol{r}) >= l_m \begin{bmatrix} \frac{1}{2A_m^+} \int_{T_m^+} \boldsymbol{A}(\boldsymbol{r}) \cdot \boldsymbol{\rho}_m^+ \, dS + \\ \frac{1}{2A_m^-} \int_{T_m^-} \boldsymbol{A}(\boldsymbol{r}) \cdot \boldsymbol{\rho}_m^- \, dS \end{bmatrix} \tag{3.17}$$

The vector potential can be obtained in terms of the convolution integral of the source current $\boldsymbol{f}_n$ and the free space Green's function. When this integral is also decomposed into two parts, for positive and negative triangles, a matrix entry involves four integrals as:

$$< \boldsymbol{w}_m, \boldsymbol{A}(\boldsymbol{r}) >= l_m \begin{bmatrix} \frac{1}{2A_m^+} \int_{T_m^+} \boldsymbol{\rho}_m^+ \cdot \frac{\mu}{4\pi} \begin{pmatrix} \int_{T_n^+} \frac{l_n}{2A_n^+} \boldsymbol{\rho}_n^+ \frac{e^{-jk|\boldsymbol{r}-\boldsymbol{r}'|}}{|\boldsymbol{r}-\boldsymbol{r}'|} dS' + \\ \int_{T_n^-} \frac{l_n}{2A_n^-} \boldsymbol{\rho}_n^- \frac{e^{-jk|\boldsymbol{r}-\boldsymbol{r}'|}}{|\boldsymbol{r}-\boldsymbol{r}'|} dS' \end{pmatrix} dS + \\ + \frac{1}{2A_m^-} \int_{T_m^-} \boldsymbol{\rho}_m^- \cdot \frac{\mu}{4\pi} \begin{pmatrix} \int_{T_n^+} \frac{l_n}{2A_n^+} \boldsymbol{\rho}_n^+ \frac{e^{-jk|\boldsymbol{r}-\boldsymbol{r}'|}}{|\boldsymbol{r}-\boldsymbol{r}'|} dS' + \\ \int_{T_n^-} \frac{l_n}{2A_n^-} \boldsymbol{\rho}_n^- \frac{e^{-jk|\boldsymbol{r}-\boldsymbol{r}'|}}{|\boldsymbol{r}-\boldsymbol{r}'|} dS' \end{pmatrix} dS \end{bmatrix} \tag{3.18}$$

Since a structured mesh is chosen, the areas of the mesh triangles are equal. Therefore, replacing all $A_n^+, A_n^-, A_m^+, A_m^-$with A and after reordering (3.18), the following equation is obtained:

$$< \boldsymbol{w}_m, \boldsymbol{A}(\boldsymbol{r}) >= \frac{\mu}{4\pi}\frac{l_m l_n}{4A^2}\begin{bmatrix} \int_{T_m^+}\int_{T_n^+} \boldsymbol{\rho}_m^+ \cdot \boldsymbol{\rho}_n^+ \frac{e^{-jk|r-r'|}}{|\boldsymbol{r}-\boldsymbol{r}'|} dS'\, dS + \\ \int_{T_m^+}\int_{T_n^-} \boldsymbol{\rho}_m^+ \cdot \boldsymbol{\rho}_n^- \frac{e^{-jk|r-r'|}}{|\boldsymbol{r}-\boldsymbol{r}'|} dS' dS + \\ \int_{T_m^-}\int_{T_n^+} \boldsymbol{\rho}_m^- \cdot \boldsymbol{\rho}_n^+ \frac{e^{-jk|r-r'|}}{|\boldsymbol{r}-\boldsymbol{r}'|} dS'\, dS + \\ \int_{T_m^-}\int_{T_n^-} \boldsymbol{\rho}_m^- \cdot \boldsymbol{\rho}_n^- \frac{e^{-jk|r-r'|}}{|\boldsymbol{r}-\boldsymbol{r}'|} dS'\, dS \end{bmatrix} \tag{3.19}$$

Then, the magnetic vector potential term of Z_{mn} can be written as:

$$j\omega < \boldsymbol{w}_m, \boldsymbol{A}(\boldsymbol{r}) >= FactorA\ (I_1 + I_2 + I_3 + I_4) \tag{3.20}$$

where,

$$FactorA = \frac{j\omega\mu}{4\pi}\frac{l_m l_n}{4A^2} \tag{3.21}$$

$$I_1 = \int_{T_m^+}\int_{T_n^+} \boldsymbol{\rho}_m^+ \cdot \boldsymbol{\rho}_n^+ \frac{e^{-jk|r-r'|}}{|\boldsymbol{r}-\boldsymbol{r}'|} dS'\, dS \tag{3.22}$$

$$I_2 = \int_{T_m^+}\int_{T_n^-} \boldsymbol{\rho}_m^+ \cdot \boldsymbol{\rho}_n^- \frac{e^{-jk|r-r'|}}{|\boldsymbol{r}-\boldsymbol{r}'|} dS' dS \tag{3.23}$$

$$I_3 = \int_{T_m^-}\int_{T_n^+} \boldsymbol{\rho}_m^- \cdot \boldsymbol{\rho}_n^+ \frac{e^{-jk|r-r'|}}{|\boldsymbol{r}-\boldsymbol{r}'|} dS'\, dS \tag{3.24}$$

$$I_4 = \int_{T_m^-}\int_{T_n^-} \boldsymbol{\rho}_m^- \cdot \boldsymbol{\rho}_n^- \frac{e^{-jk|r-r'|}}{|\boldsymbol{r}-\boldsymbol{r}'|} dS'\, dS \tag{3.25}$$

At this point, these integrals can be written according to Gaussian quadrature rule as in equation (3.5). Since, Gaussian quadrature of order 2 is used; the summation indices mpi[1], mmi[2], npi[3] and nmi[4] are incrementing until 3.

When Gaussian quadrature rule is applied, it can be seen that A^2w^2 is a common term in all integrals. Then, it can be included in the coefficient $FactorA$, leaving the $I_{1\text{-}4}$ terms only with summation.

$$FactorA = \frac{j\omega\mu}{4\pi}\frac{l_m l_n}{4}w^2 \tag{3.26}$$

---

[1] mpi: m-th RWG pair, plus triangle, quadrature point index

[2] mmi: m-th RWG pair, minus triangle, quadrature point index

[3] npi: n-th RWG pair, plus triangle, quadrature point index

[4] nmi: n-th RWG pair, minus triangle, quadrature point index

$$I_1 \cong \sum_{mpi=1}^{3} \sum_{npi=1}^{3} \boldsymbol{\rho}_{mpi}^{+} \cdot \boldsymbol{\rho}_{npi}^{+} \frac{e^{-jk\left|r_{mpi}-r'_{npi}\right|}}{\left|\boldsymbol{r}_{mpi}-\boldsymbol{r'}_{npi}\right|} \tag{3.27}$$

$$I_2 \cong \sum_{mpi=1}^{3} \sum_{nmi=1}^{3} \boldsymbol{\rho}_{mpi}^{+} \cdot \boldsymbol{\rho}_{nmi}^{-} \frac{e^{-jk\left|r_{mpi}-r'_{nmi}\right|}}{\left|\boldsymbol{r}_{mpi}-\boldsymbol{r'}_{nmi}\right|} \tag{3.28}$$

$$I_3 \cong \sum_{mmi=1}^{3} \sum_{npi=1}^{3} \boldsymbol{\rho}_{mmi}^{-} \cdot \boldsymbol{\rho}_{npi}^{+} \frac{e^{-jk\left|r_{mmi}-r'_{npi}\right|}}{\left|\boldsymbol{r}_{mmi}-\boldsymbol{r'}_{npi}\right|} \tag{3.29}$$

$$I_4 \cong \sum_{mmi=1}^{3} \sum_{nmi=1}^{3} \boldsymbol{\rho}_{mmi}^{-} \cdot \boldsymbol{\rho}_{nmi}^{-} \frac{e^{-jk\left|r_{mmi}-r'_{nmi}\right|}}{\left|\boldsymbol{r}_{mmi}-\boldsymbol{r'}_{nmi}\right|} \tag{3.30}$$

Here, the vectors $\boldsymbol{r}_{mpi}$, $\boldsymbol{r}_{mmi}$, $\boldsymbol{r'}_{npi}$ and $\boldsymbol{r'}_{nmi}$ must be calculated using the entity defined in equation (3.10). Similarly, the vectors $\boldsymbol{\rho}_{mpi}^{+}$, $\boldsymbol{\rho}_{mmi}^{-}$, $\boldsymbol{\rho}_{npi}^{+}$ and $\boldsymbol{\rho}_{nmi}^{-}$ must be calculated using the entities defined in equations (3.1) and (3.2) with the respective $\boldsymbol{r}_{mpi}$, $\boldsymbol{r}_{mmi}$, $\boldsymbol{r'}_{npi}$ and $\boldsymbol{r'}_{nmi}$.

The second term (scalar potential) of equation (3.16) can be written as:

$$< \boldsymbol{w}_m, \nabla\phi(\boldsymbol{r}) >= \int_{T_m} \boldsymbol{w}_m \cdot \nabla\phi(\boldsymbol{r}) dS \tag{3.31}$$

The scalar potential can be expressed as the convolution integral of the charge density and the free space Green's function. By relating the charge density to the divergence of the surface current, the following expression is obtained:

$$< \boldsymbol{w}_m, \nabla\phi(\boldsymbol{r}) >= -\frac{1}{4\pi\varepsilon j\omega} \int_{T_m} \boldsymbol{w}_m \cdot \nabla \int_{T_n} \nabla \cdot \boldsymbol{f}_n \frac{e^{-jk|r-r'|}}{|\boldsymbol{r}-\boldsymbol{r'}|} dS'\, dS \tag{3.32}$$

By using the vector identity $(\nabla \cdot (\varphi\boldsymbol{A}) = \varphi\nabla \cdot \boldsymbol{A} + \boldsymbol{A} \cdot \nabla\varphi)$,$\nabla$ operator can be transferred onto $\boldsymbol{w}_m$ as:

$$< \boldsymbol{w}_m, \nabla\phi(\boldsymbol{r}) >= \frac{1}{4\pi\varepsilon j\omega} \int_{T_m} \nabla \cdot \boldsymbol{w}_m \int_{T_n} \nabla \cdot \boldsymbol{f}_n \frac{e^{-jk|r-r'|}}{|\boldsymbol{r}-\boldsymbol{r'}|} dS'\, dS \tag{3.33}$$

Since $\boldsymbol{w}_m$ and $\boldsymbol{f}_n$are RWG basis functions, their divergence can be replaced by the equation (3.4), resulting in:

$$< \boldsymbol{w}_m, \nabla\phi(\boldsymbol{r}) >= \frac{1}{4\pi\varepsilon j\omega}\begin{pmatrix} \int_{T_m^+}\frac{l_m}{A_m^+}\cdot\int_{T_n^+}\frac{l_n}{A_n^+}\frac{e^{-jk|\boldsymbol{r}-\boldsymbol{r}'|}}{|\boldsymbol{r}-\boldsymbol{r}'|}dS'\,dS - \\ \int_{T_m^+}\frac{l_m}{A_m^+}\cdot\int_{T_n^-}\frac{l_n}{A_n^-}\frac{e^{-jk|\boldsymbol{r}-\boldsymbol{r}'|}}{|\boldsymbol{r}-\boldsymbol{r}'|}dS'\,dS - \\ \int_{T_m^-}\frac{l_m}{A_m^-}\cdot\int_{T_n^+}\frac{l_n}{A_n^+}\frac{e^{-jk|\boldsymbol{r}-\boldsymbol{r}'|}}{|\boldsymbol{r}-\boldsymbol{r}'|}dS'\,dS + \\ \int_{T_m^-}\frac{l_m}{A_m^-}\cdot\int_{T_n^-}\frac{l_n}{A_n^-}\frac{e^{-jk|\boldsymbol{r}-\boldsymbol{r}'|}}{|\boldsymbol{r}-\boldsymbol{r}'|}dS'\,dS \end{pmatrix} \tag{3.34}$$

Replacing area of the triangles with A, the scalar potential term of Z_{mn} can be written as:

$$< \boldsymbol{w}_m, \nabla\phi(\boldsymbol{r}) >= FactorPhi\,\left(I_{p1} + I_{p2} + I_{p3} + I_{p4}\right) \tag{3.35}$$

where,

$$FactorPhi = \frac{1}{4\pi\varepsilon j\omega}\frac{l_m l_n}{A^2} \tag{3.36}$$

$$I_{p1} = \int_{T_m^+}\int_{T_n^+}\frac{e^{-jk|\boldsymbol{r}-\boldsymbol{r}'|}}{|\boldsymbol{r}-\boldsymbol{r}'|}dS'\,dS \tag{3.37}$$

$$I_{p2} = -\int_{T_m^+}\int_{T_n^-}\frac{e^{-jk|\boldsymbol{r}-\boldsymbol{r}'|}}{|\boldsymbol{r}-\boldsymbol{r}'|}dS'\,dS \tag{3.38}$$

$$I_{p3} = -\int_{T_m^-}\int_{T_n^+}\frac{e^{-jk|\boldsymbol{r}-\boldsymbol{r}'|}}{|\boldsymbol{r}-\boldsymbol{r}'|}dS'\,dS \tag{3.39}$$

$$I_{p4} = \int_{T_m^-}\int_{T_n^-}\frac{e^{-jk|\boldsymbol{r}-\boldsymbol{r}'|}}{|\boldsymbol{r}-\boldsymbol{r}'|}dS'\,dS \tag{3.40}$$

Similarly, these integrals can be written according to Gaussian quadrature rule as in equation (3.5). Since, Gaussian quadrature of order 2 is used; the summation indices mpi, mmi, npi and nmi are incrementing until 3.

When Gaussian quadrature rule is applied, it can be seen that A^2w^2 is a common term in all integrals. Then, it can be included in the coefficient $FactorPhi$, leaving the $I_{p1\text{-}4}$ terms only with summation.

$$FactorPhi = \frac{1}{4\pi\varepsilon j\omega}l_m l_n w^2 \tag{3.41}$$

$$I_{p1} = \sum_{mpi=1}^{3}\sum_{npi=1}^{3}\frac{e^{-jk|\boldsymbol{r}_{mpi}-\boldsymbol{r}'_{npi}|}}{|\boldsymbol{r}_{mpi}-\boldsymbol{r}'_{npi}|} \tag{3.42}$$

$$I_{p2} = -\sum_{mpi=1}^{3}\sum_{nmi=1}^{3}\frac{e^{-jk|\boldsymbol{r}_{mpi}-\boldsymbol{r}'_{nmi}|}}{|\boldsymbol{r}_{mpi}-\boldsymbol{r}'_{nmi}|} \tag{3.43}$$

$$I_{p3} = -\sum_{mmi=1}^{3}\sum_{npi=1}^{3}\frac{e^{-jk|\boldsymbol{r}_{mmi}-\boldsymbol{r}'_{npi}|}}{|\boldsymbol{r}_{mmi}-\boldsymbol{r}'_{npi}|} \tag{3.44}$$

$$I_{p4} = \sum_{mmi=1}^{3}\sum_{nmi=1}^{3}\frac{e^{-jk|\boldsymbol{r}_{mmi}-\boldsymbol{r}'_{nmi}|}}{|\boldsymbol{r}_{mmi}-\boldsymbol{r}'_{nmi}|} \tag{3.45}$$

Here, the vectors $\boldsymbol{r}_{mpi}$, $\boldsymbol{r}_{mmi}$, $\boldsymbol{r}'_{npi}$ and $\boldsymbol{r}'_{nmi}$ must be calculated using the entity defined in equation (3.10).

3.4 SINGULARITY HANDLING AND RESULTS

In the implementation of Method of Moments, a singularity problem occurs when the basis and the testing triangles are the same and the Gaussian quadrature points coincide. Since the RWG function consists of two triangular patches, a singularity occurs even when the neighboring RWG pairs are selected. Figure 10 shows such an example.

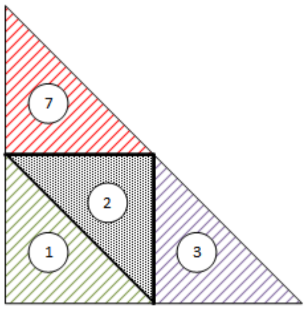

Figure 10 - RWG pairs

In Figure 10, 3 RWG pairs are visible; the first RWG pair consists of the triangles T#7 and T#2, the second RWG pair consists of the triangles T#3 and T#2 and the last RWG pair consists of the triangles T#1 and T#2. As it can be seen, all RWG pairs share a common triangle: T#2. Therefore, not only the interactions of self RWG pairs but also neighboring RWG pairs result in a singularity case.

There are several methods to overcome this singularity problem in a triangular meshed structure. In this thesis, two methods are applied. The first method is used in the book [6] by S. Makarov and the second method is called the Direct Evaluation Method and suggested by A. Polimeridis in [7].

In this chapter, both singularity handling methods will be explained.

In the method proposed by Makarov [6], to avoid the singularity problem, different Gauss quadrature orders are used for source and testing integrals, so that source and observation points do not coincide.

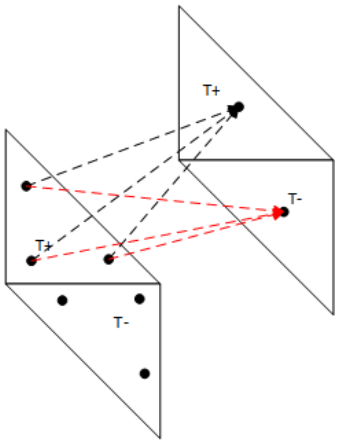

Figure 11 - r vectors for two RWG pairs (Makarov)

Figure 11 demonstrates this approach. Testing is performed at a single point (centroid), whereas source integral is calculated by using 3-points.

Then, the elements of equation (3.20) become:

$$FactorA = \frac{j\omega\mu}{4\pi}\frac{l_m l_n}{4}w \tag{3.46}$$

$$I_1 \cong \sum_{mpi=1}^{3}\sum_{npi=1}^{1}\boldsymbol{\rho}_{mpi}^{+}\cdot\boldsymbol{\rho}_{npi}^{+}\frac{e^{-jk\left|r_{mpi}-r'_{npi}\right|}}{\left|\boldsymbol{r}_{mpi}-\boldsymbol{r}'_{npi}\right|} \tag{3.47}$$

$$I_2 \cong \sum_{mpi=1}^{3}\sum_{nmi=1}^{1}\boldsymbol{\rho}_{mpi}^{+}\cdot\boldsymbol{\rho}_{nmi}^{-}\frac{e^{-jk\left|r_{mpi}-r'_{nmi}\right|}}{\left|\boldsymbol{r}_{mpi}-\boldsymbol{r}'_{nmi}\right|} \tag{3.48}$$

$$I_3 \cong \sum_{mmi=1}^{3}\sum_{npi=1}^{1}\boldsymbol{\rho}_{mmi}^{-}\cdot\boldsymbol{\rho}_{npi}^{+}\frac{e^{-jk\left|r_{mmi}-r'_{npi}\right|}}{\left|\boldsymbol{r}_{mmi}-\boldsymbol{r}'_{npi}\right|} \tag{3.49}$$

$$I_4 \cong \sum_{mmi=1}^{3}\sum_{nmi=1}^{1}\boldsymbol{\rho}_{mmi}^{-}\cdot\boldsymbol{\rho}_{nmi}^{-}\frac{e^{-jk\left|r_{mmi}-r'_{nmi}\right|}}{\left|\boldsymbol{r}_{mmi}-\boldsymbol{r}'_{nmi}\right|} \tag{3.50}$$

Similarly, the elements of equation (3.35) become:

$$FactorPhi = \frac{1}{4\pi\varepsilon j\omega}l_m l_n w \tag{3.51}$$

$$I_{p1} = \sum_{mpi=1}^{3} \sum_{npi=1}^{1} \frac{e^{-jk\left|r_{mpi}-r'_{npi}\right|}}{\left|\boldsymbol{r}_{mpi}-\boldsymbol{r}'_{npi}\right|} \tag{3.52}$$

$$I_{p2} = -\sum_{mpi=1}^{3} \sum_{nmi=1}^{1} \frac{e^{-jk\left|r_{mpi}-r'_{nmi}\right|}}{\left|\boldsymbol{r}_{mpi}-\boldsymbol{r}'_{nmi}\right|} \tag{3.53}$$

$$I_{p3} = -\sum_{mmi=1}^{3} \sum_{npi=1}^{1} \frac{e^{-jk\left|r_{mmi}-r'_{npi}\right|}}{\left|\boldsymbol{r}_{mmi}-\boldsymbol{r}'_{npi}\right|} \tag{3.54}$$

$$I_{p4} = \sum_{mmi=1}^{3} \sum_{nmi=1}^{1} \frac{e^{-jk\left|r_{mmi}-r'_{nmi}\right|}}{\left|\boldsymbol{r}_{mmi}-\boldsymbol{r}'_{nmi}\right|} \tag{3.55}$$

It should be noted that, this is not a very accurate approach. However, in [6] it is demonstrated that the error introduced in this method is acceptable as long as scattering problems are concerned. On the other hand, if one needs an improved accuracy, singularity subtraction [11] or cancellation [12] methods must be utilized.

Basically singularity subtraction method suggests the subtraction of the singular part from the integral and evaluating this analytically [11]. On the other hand, in singularity cancellation methods a suitable transformation is applied, so that the Jacobian of the transformation cancels the singularity. Then, the transformed integral can be evaluated numerically. Duffy's method [13] and double exponential method [14] are most widely used singularity cancellation techniques.

Recently, a direct evaluation method [7], [23] is proposed that does not require any numerical integration. In this method, when a series of singularity cancellation, reordering of integrations and one analytical integration is applied, the results become sufficiently smooth that makes a straightforward computation using Gaussian quadrature rule possible [7]. The MatLab library that implements this method is available in the world-wide-web [15] together with explanatory instructions about the use of related source files. A short note about the use of these open source codes is given in Appendix.

When direct evaluation method library (DEMCEM) is used, the interaction between 2 RWG pairs is calculated as shown in Figure 12.

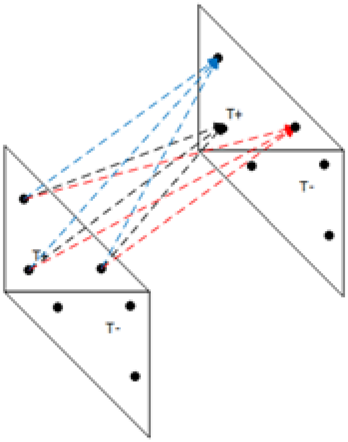

Figure 12 - r vectors for two RWG pairs

The formulation presented in this chapter is implemented to analyze scattering from square PEC plates of length $\lambda \times \lambda$ and $2\lambda \times 2\lambda$. The plate is assumed to be in the $xy - plane$. Three different ($x - polarized$, $y - polarized$ and $xy - polarized$ with normal incidence) plane wave excitations are considered. To handle the singularity both the method suggested by Makarov and DEMCEM are utilized. Step size of λ/8 is chosen in both axes that results in $8 \times 16 = 128$ triangles. The current distribution on the $\lambda \times \lambda$ plate is presented for the Makarov's approach and for DEMCEM in Figure 13 and Figure 14, respectively. It can be observed that even the shape of the current distribution looks similar in both approaches; the current magnitudes exhibit a slide difference due to the improved accuracy offered by DEMCEM.

<table>
<tr><th>Surface current distribution</th><th>Surface current flow directions</th></tr>
<tr><td>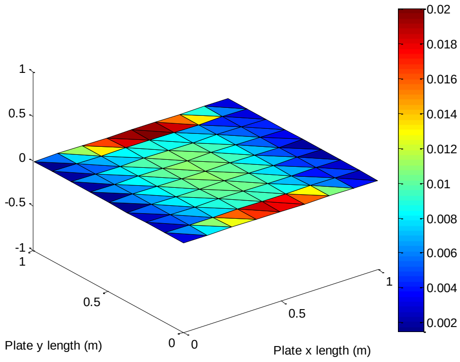
</td><td>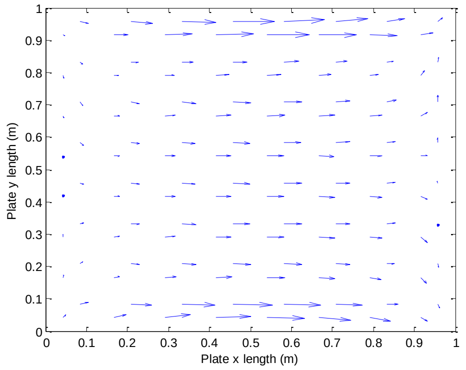
</td></tr>
<tr><td colspan="2">$x - polarized$ incidence
Maximum surface current on the plate $J_{max} = 0.020$ [A/m]</td></tr>
<tr><td>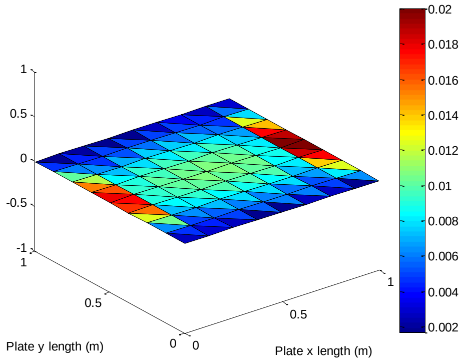
</td><td>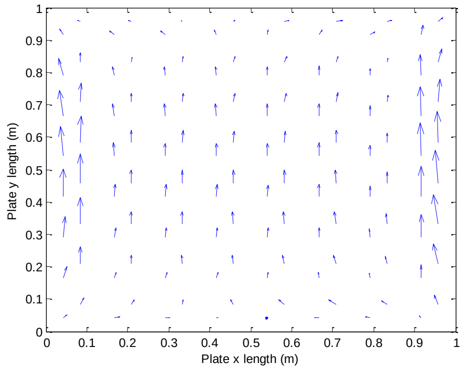
</td></tr>
<tr><td colspan="2">$y - polarized$ incidence
Maximum surface current on the plate $J_{max} = 0.020$ [A/m]</td></tr>
<tr><td>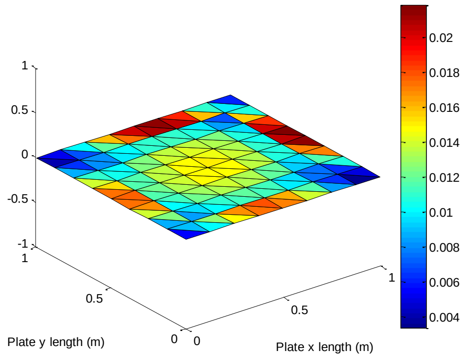
</td><td>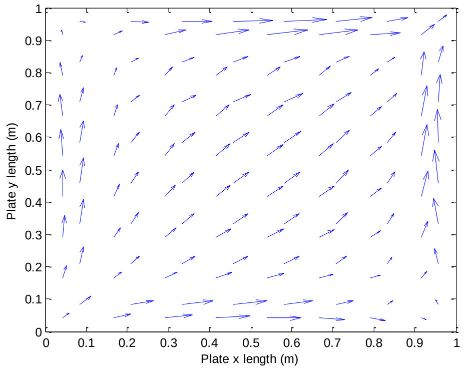
</td></tr>
<tr><td colspan="2">$xy - polarized$ incidence
Maximum surface current on the plate $J_{max} = 0.022$ [A/m]</td></tr>
</table>

Figure 13 - Surface current distribution on λ x λ plate using Makarov's method

<table>
<tr><th>Surface current distribution</th><th>Surface current flow directions</th></tr>
<tr><td>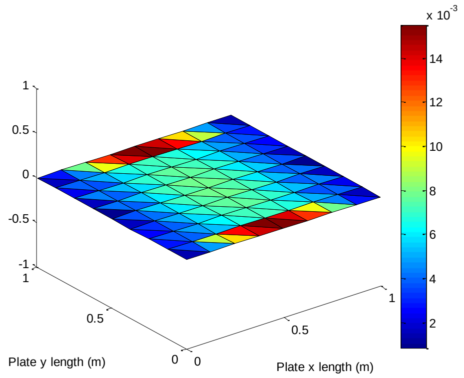 </td><td>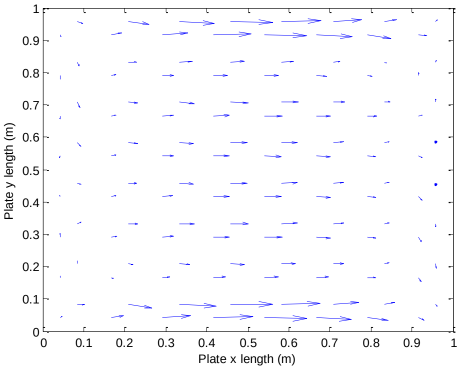 </td></tr>
<tr><td colspan="2">$x - polarized$ incidence
Maximum surface current on the plate $J_{max} = 0.015$ [A/m]</td></tr>
<tr><td>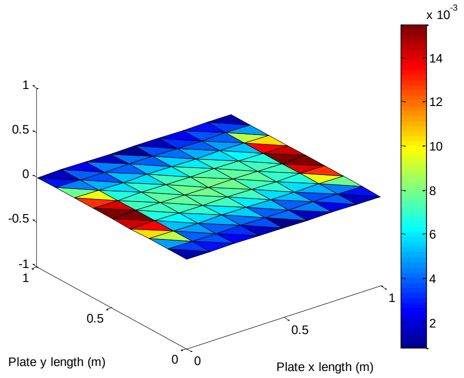 </td><td>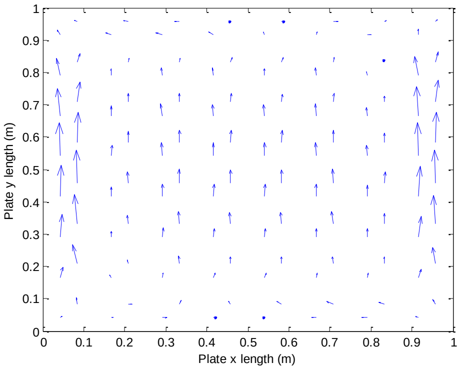 </td></tr>
<tr><td colspan="2">$y - polarized$ incidence
Maximum surface current on the plate $J_{max} = 0.015$ [A/m]</td></tr>
<tr><td>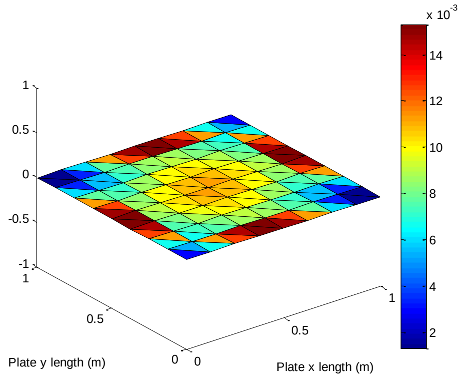 </td><td>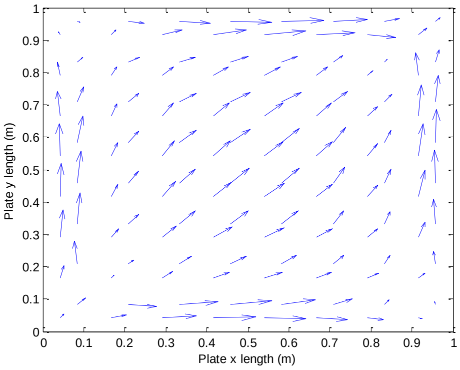 </td></tr>
<tr><td colspan="2">$xy - polarized$ incidence
Maximum surface current on the plate $J_{max} = 0.015$ [A/m]</td></tr>
</table>

Figure 14 - Surface current distribution on λ x λ plate using DEMCEM

Similarly, the current distribution on the 2λ x 2λ plate is presented for the Makarov's approach and for DEMCEM in Figure 15 and Figure 16, respectively. When the size of the plate is increased to 2λ, the higher order modes excited on the plate can be observed from the current distribution plots.

<table>
<tr><th>Surface current distribution</th><th>Surface current flow directions</th></tr>
<tr><td>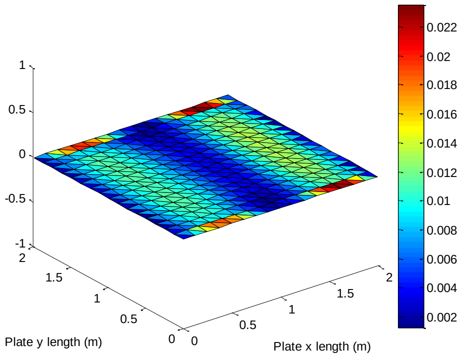
</td><td>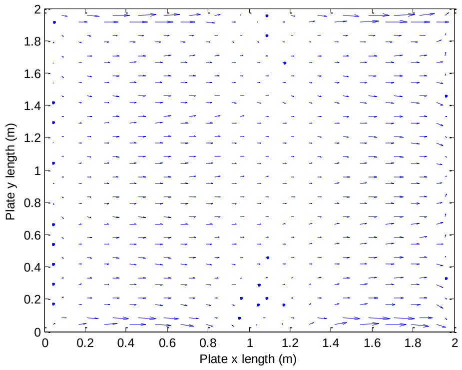
</td></tr>
<tr><td colspan="2">$x-polarized$ incidence
Maximum surface current on the plate $J_{max} = 0.023$ [A/m]</td></tr>
<tr><td>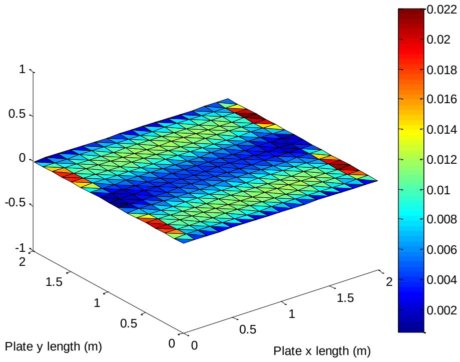
</td><td>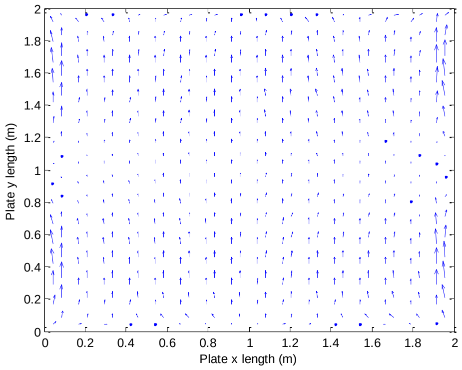
</td></tr>
<tr><td colspan="2">$y-polarized$ incidence
Maximum surface current on the plate $J_{max} = 0.022$ [A/m]</td></tr>
<tr><td>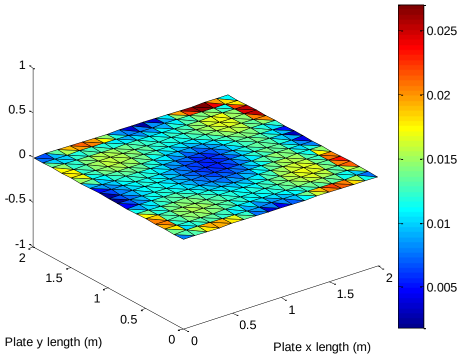
</td><td>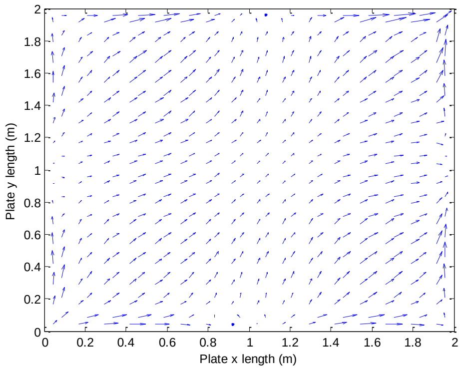
</td></tr>
<tr><td colspan="2">$xy-polarized$ incidence
Maximum surface current on the plate $J_{max} = 0.027$ [A/m]</td></tr>
</table>

Figure 15 - Surface current distribution on 2λ x 2λ plate using Makarov's method

<table>
<tr><th>Surface current distribution</th><th>Surface current flow directions</th></tr>
<tr><td>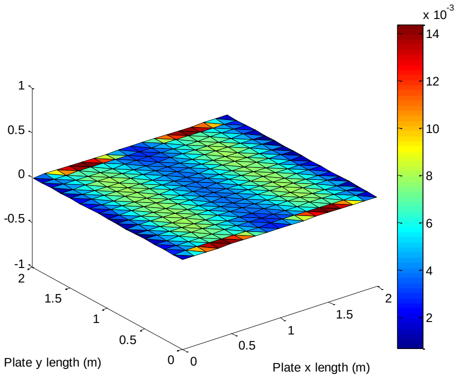
</td><td>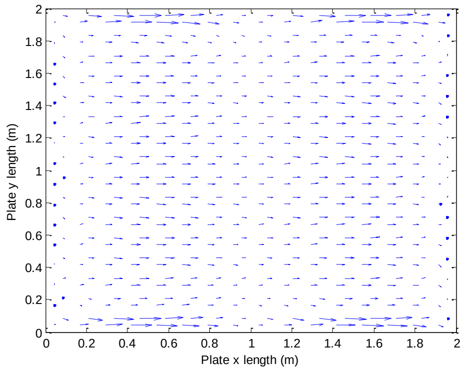
</td></tr>
<tr><td colspan="2">$x - polarized$ incidence
Maximum surface current on the plate $J_{max} = 0.014$ [A/m]</td></tr>
<tr><td>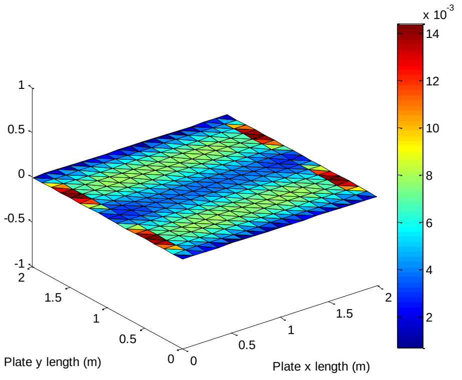
</td><td>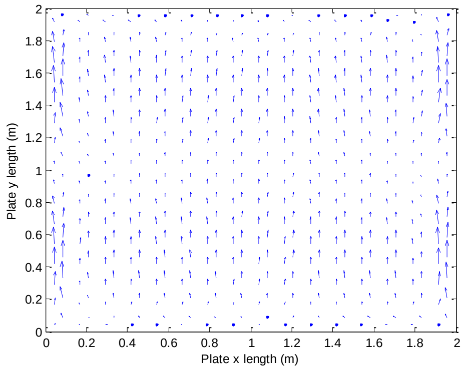
</td></tr>
<tr><td colspan="2">$y - polarized$ incidence
Maximum surface current on the plate $J_{max} = 0.014$ [A/m]</td></tr>
<tr><td>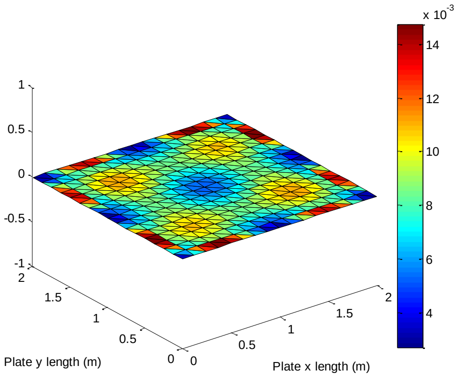
</td><td>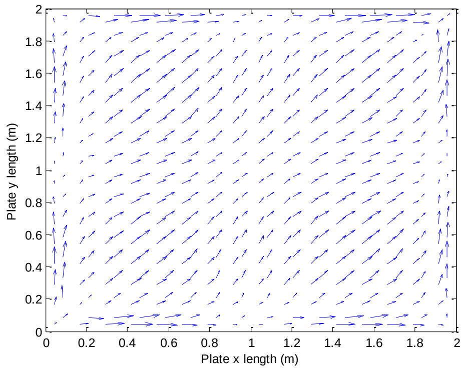
</td></tr>
<tr><td colspan="2">$xy - polarized$ incidence
Maximum surface current on the plate $J_{max} = 0.015$ [A/m]</td></tr>
</table>

Figure 16 - Surface current distribution on 2λ x 2λ plate using DEMCEM

CHAPTER 4

MoM ANALYSIS OF THIN WIRES

In the previous chapter the conducting plate was assumed to be in the $xy-plane$. In later chapters, the thin wire will be considered to be orthogonal to the plate. So, the wire is oriented in z-direction.

In this chapter, the MoM formulation for a z-directed thin wire will be presented. The integral equation is same as the integral equation considered in the previous chapter. The only difference is the reduction in the size of the problem. Since, the current density is a function of z only, the gradient operator can be simply replaced by $d/_{dz}$. Moreover, it should be noted that instead of the Green's function for a cylindrical wire of radius a, approximate Green's function that assumes the current to be concentrated at the axis of the cylinder is utilized due to the thin wire assumption.

The MoM formulation starts with the choice of the basis function. Recall from the previous chapter that to compute the scalar potential, the gradient of the basis function is required. Hence, the basis function should be piecewise differentiable. Piecewise sinusoidal functions are widely used in the analysis of the thin wire antennas. However, piecewise linear (triangular) functions are preferred in this study, since they are found to be more compatible with RWG basis functions, which are linear functions as well. The triangular basis functions are defined as:

$$\mathbf{\Lambda}_n = \Lambda_n(z')\hat{\boldsymbol{a}}_z$$

where,

$$\Lambda_n(z') = \begin{cases} \frac{z'-z_{n-1}}{z_n-z_{n-1}}, & z_{n-1} \le z' \le z_n \\ \frac{z_{n+1}-z'}{z_{n+1}-z_n}, & z_n \le z' \le z_{n+1} \end{cases} \qquad (4.1)$$

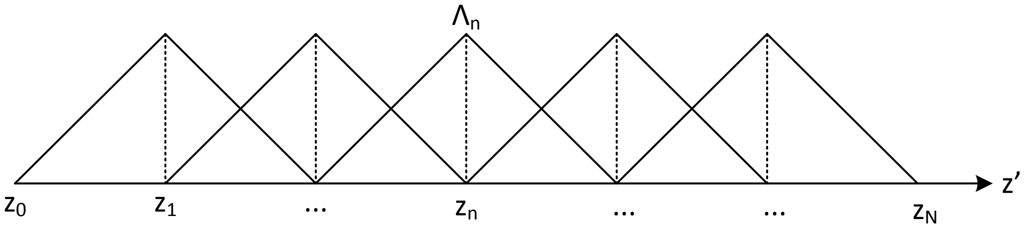

Figure 17 - Piecewise linear (triangular) basis functions

and the divergence of the triangular basis function is:

$$\nabla \cdot \boldsymbol{\Lambda}_n(z') = \begin{cases} \frac{1}{z_n - z_{n-1}}, & z_{n-1} \le z' \le z_n \\ \frac{-1}{z_{n+1} - z_n}, & z_n \le z' \le z_{n+1} \end{cases} \tag{4.2}$$

Recall from the previous chapter that the impedance matrix Z_{mn} is can be expressed as:

$$Z_{mn} = j\omega < \boldsymbol{w}_m, \boldsymbol{A}(\boldsymbol{r}) > + < \boldsymbol{w}_m, \boldsymbol{\nabla}\phi(\boldsymbol{r}) > \tag{4.3}$$

The vector potential part of the impedance matrix Z_{mn} can be written for Galerkin testing with triangular basis function as:

$$< \boldsymbol{w}_m, \boldsymbol{A}(\boldsymbol{r}) >= \int_{W_m} \Lambda_m \frac{\mu}{4\pi} \int_{W_n} \Lambda_n \frac{e^{-jk|z-z'|}}{|\boldsymbol{z}-\boldsymbol{z}'|} dz dz' \tag{4.4}$$

Since the triangular basis function is a partially continuous function, each integration can be divided into 2 parts resulting in totally 4 integrals:

$$< \boldsymbol{w}_m, \boldsymbol{A}(\boldsymbol{r}) >= FactorA_w(I_{w1} + I_{w2} + I_{w3} + I_{w4}) \tag{4.5}$$

where,

$$FactorA_w = \frac{j\omega\mu}{4\pi} \tag{4.6}$$

$$I_{w1} = \int_{z_{m-1}}^{z_m} \int_{z_{n-1}}^{z_n} \frac{z - z_{m-1}}{z_m - z_{m-1}} \frac{z' - z_{n-1}}{z_n - z_{n-1}} \frac{e^{-jk|z-z'|}}{|z-z'|} dz' dz \tag{4.7}$$

$$I_{w2} = \int_{z_{m-1}}^{z_m} \int_{z_n}^{z_{n+1}} \frac{z - z_{m-1}}{z_m - z_{m-1}} \frac{z_{n+1} - z'}{z_{n+1} - z_n} \frac{e^{-jk|z-z'|}}{|z-z'|} dz' dz \tag{4.8}$$

$$I_{w3} = \int_{z_m}^{z_{m+1}} \int_{z_{n-1}}^{z_n} \frac{z_{m+1} - z}{z_{m+1} - z_m} \frac{z' - z_{n-1}}{z_n - z_{n-1}} \frac{e^{-jk|z-z'|}}{|z-z'|} dz' dz \tag{4.9}$$

$$I_{w4} = \int_{z_m}^{z_{m+1}} \int_{z_n}^{z_{n+1}} \frac{z_{m+1}-z}{z_{m+1}-z_m} \frac{z_{n+1}-z'}{z_{n+1}-z_n} \frac{e^{-jk|z-z'|}}{|z-z'|} dz' dz \tag{4.10}$$

Similarly, the scalar potential part takes the following form after transferring the gradient operator onto the testing function:

$$< \boldsymbol{w}_m, \boldsymbol{\nabla}\phi(\boldsymbol{r}) >= \frac{1}{4\pi\varepsilon j\omega} \int_{W_m} \nabla \cdot \boldsymbol{\Lambda}_m \int_{W_n} \nabla \cdot \boldsymbol{\Lambda}_n \frac{e^{-jk|z-z'|}}{|z-z'|} dz' dz \tag{4.11}$$

This term is divided into 4 parts as well:

$$< \boldsymbol{w}_m, \boldsymbol{\nabla}\phi(\boldsymbol{r}) >= FactorPhi_w \left(I_{pw1} + I_{pw2} + I_{pw3} + I_{pw4} \right) \tag{4.12}$$

where,

$$FactorPhi_w = \frac{1}{4\pi\varepsilon j\omega} \tag{4.13}$$

$$I_{w1} = \int_{z_{m-1}}^{z_m} \int_{z_{n-1}}^{z_n} \frac{1}{z_m - z_{m-1}} \frac{1}{z_n - z_{n-1}} \frac{e^{-jk|z-z'|}}{|z-z'|} dz' dz \tag{4.14}$$

$$I_{w2} = \int_{z_{m-1}}^{z_m} \int_{z_n}^{z_{n+1}} \frac{1}{z_m - z_{m-1}} \frac{-1}{z_{n+1} - z_n} \frac{e^{-jk|z-z'|}}{|z-z'|} dz' dz \tag{4.15}$$

$$I_{w3} = \int_{z_m}^{z_{m+1}} \int_{z_{n-1}}^{z_n} \frac{-1}{z_{m+1} - z_m} \frac{1}{z_n - z_{n-1}} \frac{e^{-jk|z-z'|}}{|z-z'|} dz' dz \tag{4.16}$$

$$I_{w4} = \int_{z_m}^{z_{m+1}} \int_{z_n}^{z_{n+1}} \frac{-1}{z_{m+1} - z_m} \frac{-1}{z_{n+1} - z_n} \frac{e^{-jk|z-z'|}}{|z-z'|} dz' dz \tag{4.17}$$

4.1 SINGULARITY HANDLING

For all non-overlapping segments, the integrals found in the previous chapter are evaluated numerically. When the chosen segments overlap, singularity problem occurs. To overcome this problem, the method proposed in [8] is utilized. This method relies on the fact that if pulse type basis functions are used instead of triangular, the integrals involved in the entries of MoM matrix can be evaluated analytically. To make use of this fact, the triangular basis function is divided into 6 subsegments as shown in Figure 18 and the constant value of each subsegment is assumed to be equal to the value of the triangular function at the center of the corresponding subsegment.

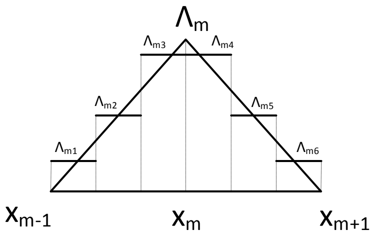

Figure 18 - Staircase approximation of the triangular function

For the computation of a self term, which is the interaction of a triangle with itself, 6x6=36 interactions of subsegments need to be calculated. When the subsegments do not overlap, the integrals found in the previous section are evaluated numerically. For overlapping sub-segments, the integral of the Green's function can be approximated analytically [8].

$$\psi = \int_{\Delta z}\int_{\Delta z} G(\boldsymbol{r},\boldsymbol{r}')\, dz'dz = \frac{1}{4\pi}\int_{\Delta z}\int_{\Delta z}\frac{e^{-jkR}}{R}dz'dz \qquad (4.18)$$

Here, Δz denotes the length of the subsegment and $R = |\boldsymbol{r} - \boldsymbol{r}'| = \sqrt{a^2 + (z - z')^2}$, where a is the radius of the dipole. When thin wire approximation is used, the basis function is placed on the surface of the dipole whereas the testing function is placed on the axis of the dipole (in this case z-axis).

Expanding the equation (4.18) into a Maclaurin series:

$$\psi = \frac{1}{4\pi}\int_{\Delta z}\int_{\Delta z}\frac{1}{R} - jk - \frac{k^2}{2}R + \ldots dz'dz \qquad (4.19)$$

Ignoring the higher order terms, the equation (4.19) is evaluated as [8]:

$$\psi = \frac{\Delta z}{2\pi}\left[ln\left(\frac{\Delta z}{a} + \sqrt{1 + \left(\frac{\Delta z}{a}\right)^2}\right) - \sqrt{1 + \left(\frac{a}{\Delta z}\right)^2} + \frac{a}{\Delta z}\right] - \frac{jk}{4\pi}\Delta z^2 \qquad (4.20)$$

4.2 SIMULATION RESULTS

Using the approach presented in this chapter, dipole antennas of different length ($\frac{\lambda}{4}$, $\frac{\lambda}{2}$, λ and $\frac{3\lambda}{2}$) are analysed with different number of basis functions to observe the convergence of the results. The dipole is excited with a delta-gap voltage source of 1V. The current distribution on the $\frac{\lambda}{2}$ dipole antenna is shown in Figure 19. In the following figure legends "points" refer to the number of basis functions.

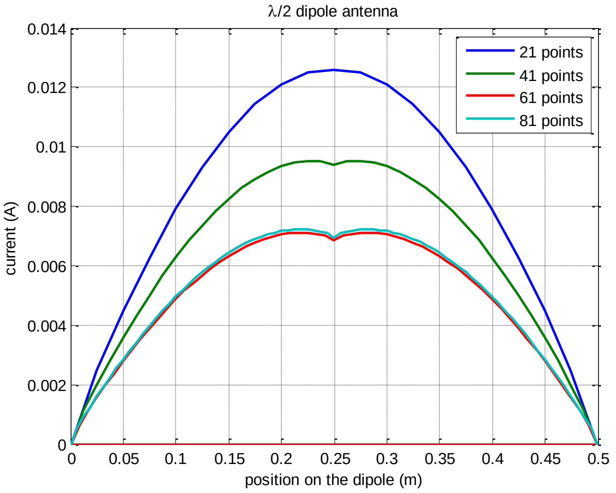

Figure 19 - Current distribution on a $\lambda/2$ dipole

The comparison between the results with respect to the number of basis functions show that the results of the simulation converge when the number of basis functions is around 60-80. The convergence may be obtained with a much smaller number of basis functions if other basis functions like piecewise sinusoidal are used. The slow convergence associated with the triangular basis function is due to the abrupt changing behavior that gives rise to a deficiency in modeling the true currents and also due to the approximate method used in handling the singularity situation. However, triangular basis functions are preferred in this study, since they comply with the attachment mode that will be introduced at the junction. The results for $\frac{\lambda}{4}$, λ and $\frac{3\lambda}{2}$ are shown in Figure 20, Figure 21 and Figure 22.

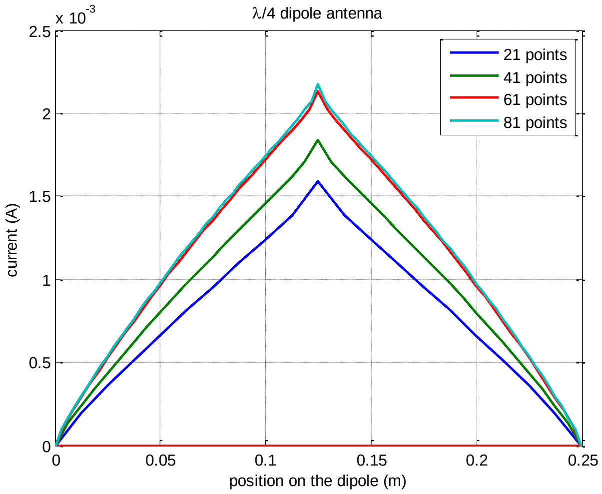

Figure 20 - Current distribution on a $\lambda/4$ dipole

As the length of the dipole becomes shorter than half wavelength, the current starts to vary more abruptly and a triangular-like current distribution occurs.

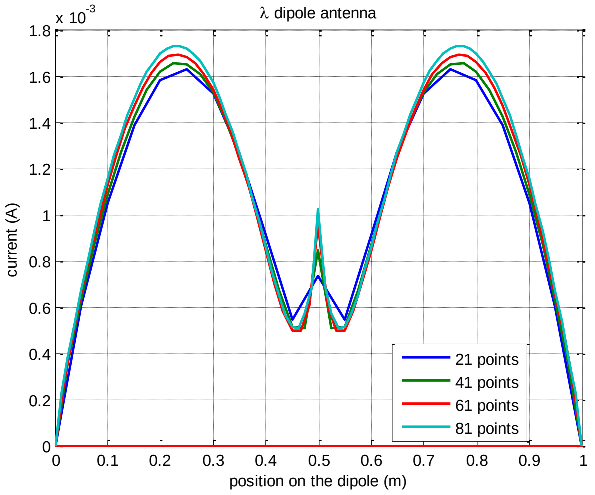

Figure 21 - Current distribution on a λ dipole

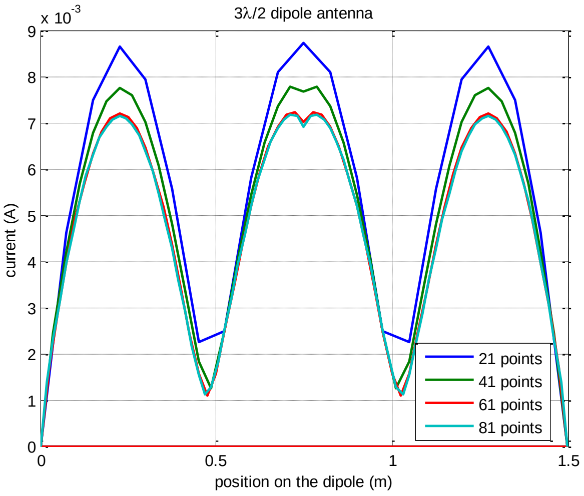

Figure 22 - Current distribution on a $3\lambda/2$ dipole

The higher order modes excited on dipoles longer than half wavelength can be observed in Figure 21 and Figure 22. Moreover, the results for 21 basis functions become less accurate as the length of the dipole increases.

CHAPTER 5

MOM ANALYSIS OF NON-CONTACTING SURFACES AND WIRES

So far, the PEC plate and thin wire are analyzed separately. In this chapter, the plate and the wire will be considered in a non-contacting configuration as shown in Figure 23 and they will be analyzed together by taking the interaction between them into account.

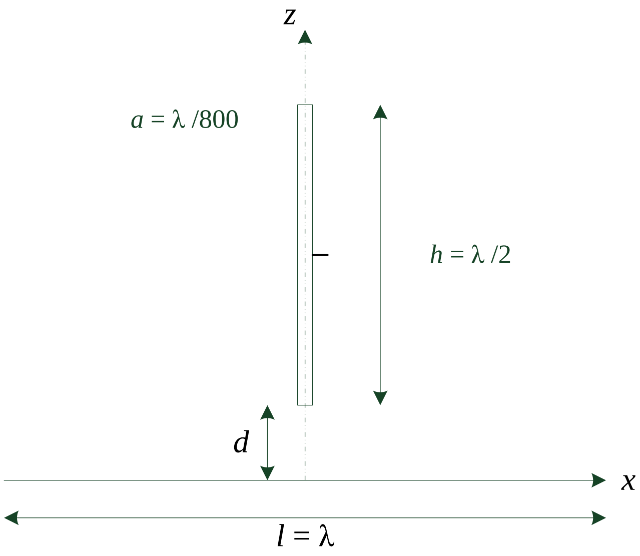

Figure 23 - Non-contacting configuration of thin wire and plate

The currents on the wire will result in a field on the plate and the currents on the plate will give rise to a field on the wire. As a result of these additional field components, the MoM matrix equation for the current coefficients on the plate ($\boldsymbol{I}_P$) and on the wire ($\boldsymbol{I}_W$), takes the following form:

$$\begin{bmatrix} \boldsymbol{Z}_{PP} & \boldsymbol{C}_{PW} \\ \boldsymbol{C}_{WP} & \boldsymbol{Z}_{WW} \end{bmatrix} \begin{bmatrix} \boldsymbol{I}_P \\ \boldsymbol{I}_W \end{bmatrix} = \begin{bmatrix} \boldsymbol{V}^P \\ \boldsymbol{V}^W \end{bmatrix} \qquad (5.1)$$

Here, $\boldsymbol{Z}_{WW}$ is the impedance matrix of the wire and $\boldsymbol{V}^W$ is the excitation vector found in Chapter 4. Similarly, $\boldsymbol{Z}_{PP}$ is the impedance matrix of the plate and $\boldsymbol{V}^P$ is the excitation vector found in Chapter 3. The matrices $\boldsymbol{C}_{WP}$ and $\boldsymbol{C}_{PW}$ are referred as coupling matrices. $\boldsymbol{C}_{WP}$ define the electric field on the wire due to the current on the plate and vice-versa.

The overall system matrix still holds the Galerkin property (being a symmetrical matrix). Therefore, $\boldsymbol{C}_{PW}$=${\boldsymbol{C}_{WP}}^T$ so $\boldsymbol{C}_{PW}$ is evaluated first and $\boldsymbol{C}_{WP}$ is obtained by taking the transpose of this matrix. The electric field on the plate due to the currents on the wire ($\boldsymbol{E}^{P,W}$) can be written as:

$$\boldsymbol{E}^{P,W} = -j\omega\boldsymbol{A}(\boldsymbol{r}) - \nabla\phi(\boldsymbol{r}) \tag{5.2}$$

$$\boldsymbol{A}(\boldsymbol{r}) = \frac{\mu}{4\pi}\int_{W_n}\boldsymbol{\Lambda}_n\frac{e^{-jk|r-r'|}}{|\boldsymbol{r}-\boldsymbol{r}'|}dz' \tag{5.3}$$

$$\phi(\boldsymbol{r}) = -\frac{1}{4\pi j\omega\varepsilon}\int_{W_n}(\nabla\cdot\boldsymbol{\Lambda}_n)\frac{e^{-jk|r-r'|}}{|\boldsymbol{r}-\boldsymbol{r}'|}dz' \tag{5.4}$$

$$\boldsymbol{r} = x\hat{\boldsymbol{a}}_x + y\hat{\boldsymbol{a}}_y \text{ and } \boldsymbol{r}' = z'\hat{\boldsymbol{a}}_z \tag{5.5}$$

The coupling matrix C_{PW} can be written as:

$$C_{PW} =< \boldsymbol{w}_m, \boldsymbol{E}_n^{P,W} >= -j\omega < \boldsymbol{w}_m, \boldsymbol{A}(\boldsymbol{r}) > -< \boldsymbol{w}_m, \nabla\phi(\boldsymbol{r}) > \tag{5.6}$$

where, $\boldsymbol{w}_m$ denotes the RWG basis functions.

The first term of the equation (5.6) can be written as:

$$-j\omega < \boldsymbol{w}_m, \boldsymbol{A}(\boldsymbol{r}) >= \frac{-j\omega l_m}{2A_m}\frac{\mu}{4\pi}\begin{bmatrix}\int_{T_m^+}\int_{W_n}(\boldsymbol{\rho}_m^+\cdot\boldsymbol{\Lambda}_n)\frac{e^{-jk|r-r'|}}{|\boldsymbol{r}-\boldsymbol{r}'|}dz'\,dS + \\ \int_{T_m^-}\int_{W_n}(\boldsymbol{\rho}_m^-\cdot\boldsymbol{\Lambda}_n)\frac{e^{-jk|r-r'|}}{|\boldsymbol{r}-\boldsymbol{r}'|}dz'\,dS\end{bmatrix} \tag{5.7}$$

Here, it can be seen that the equation (5.7) diminishes. This is because, the vectors of the RWG functions $\boldsymbol{\rho}_m^+$ and $\boldsymbol{\rho}_m^-$ have components in x-y plane, whereas the piecewise linear basis function $\boldsymbol{\Lambda}_n$ has components only in z- direction. Therefore, the dot product of these two vectors is 0.

After transferring the gradient operator onto the testing function, the scalar potential term of C_{PW} can be written as:

$$< \boldsymbol{w}_m, \nabla\phi(\boldsymbol{r}) >= \frac{1}{4\pi j\omega\varepsilon}\begin{pmatrix}\int_{T_m^+}(\nabla\cdot\boldsymbol{w}_m)\int_{W_n}(\nabla\cdot\boldsymbol{\Lambda}_n)\frac{e^{-jk|r-r'|}}{|\boldsymbol{r}-\boldsymbol{r}'|}dz'\,dS + \\ \int_{T_m^-}(\nabla\cdot\boldsymbol{w}_m)\int_{W_n}(\nabla\cdot\boldsymbol{\Lambda}_n)\frac{e^{-jk|r-r'|}}{|\boldsymbol{r}-\boldsymbol{r}'|}dz'\,dS\end{pmatrix} \tag{5.8}$$

Substituting the values for $(\nabla \cdot \boldsymbol{w}_m)$ and $(\nabla \cdot \boldsymbol{\Lambda}_n)$ and reordering the equation (5.8) yields:

$$< \boldsymbol{w}_m, \nabla\phi(\boldsymbol{r}) >= \begin{bmatrix} \frac{1}{4\pi j\omega\varepsilon}\begin{pmatrix} \frac{l_m}{A_m}\frac{1}{z_n - z_{n-1}}\int_{T_m^+}\int_{z_{n-1}}^{z_n}\frac{e^{-jk|r-r'|}}{|\boldsymbol{r}-\boldsymbol{r}'|}dz'\,dS + \\ \frac{-l_m}{A_m}\frac{1}{z_n - z_{n-1}}\int_{T_m^-}\int_{z_{n-1}}^{z_n}\frac{e^{-jk|r-r'|}}{|\boldsymbol{r}-\boldsymbol{r}'|}dz'\,dS \end{pmatrix} + \\ \frac{1}{4\pi j\omega\varepsilon}\begin{pmatrix} \frac{l_m}{A_m}\frac{-1}{z_{n+1} - z_n}\int_{T_m^+}\int_{z_n}^{z_{n+1}}\frac{e^{-jk|r-r'|}}{|\boldsymbol{r}-\boldsymbol{r}'|}dz'\,dS + \\ \frac{-l_m}{A_m}\frac{-1}{z_{n+1} - z_n}\int_{T_m^-}\int_{z_n}^{z_{n+1}}\frac{e^{-jk|r-r'|}}{|\boldsymbol{r}-\boldsymbol{r}'|}dz'\,dS \end{pmatrix} \end{bmatrix} \quad (5.9)$$

For the numerical evaluation of the integrals in the equation (5.9), Gaussian quadrature of order 2 for the triangular patch and Gaussian integration with 4 points for the line integral is used.

5.1 SIMULATION RESULTS

Two different configurations are considered. In the first configuration, a center fed half wavelength dipole antenna on the conducting plate is considered. In the second configuration, a quarter wavelength monopole fed from the edge close to the PEC plate is considered. For both configurations size of the PEC plate is chosen to be $\lambda \times \lambda$ and the feed is modelled with a delta-gap generator. The absolute value of the current for two different distance values (*d*) between the vertical wire and plate (Figure 23) is obtained from the simulation and compared with the results from FeKo in Figure 24 through Figure 27.

<table>
<tr><td>Configuration:</td><td>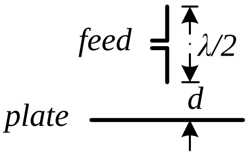
</td></tr>
<tr><td colspan="2">Current distribution on the dipole</td></tr>
<tr><td>Simulation results</td><td>FeKo simulation results</td></tr>
<tr><td>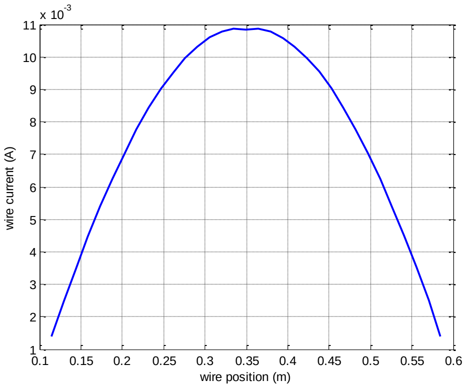
</td><td>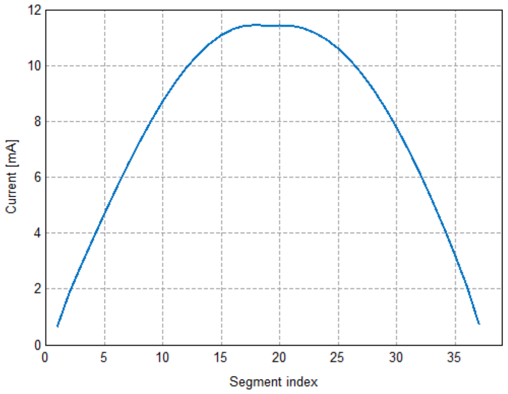
</td></tr>
<tr><td>Maximum current on the wire
$I_{max} = 10.9$ [mA].</td><td>Maximum current on the wire
$I_{max} = 11.7$ [mA].</td></tr>
<tr><td colspan="2">Surface current distribution on the plate</td></tr>
<tr><td>Simulation results</td><td>FeKo simulation results</td></tr>
<tr><td>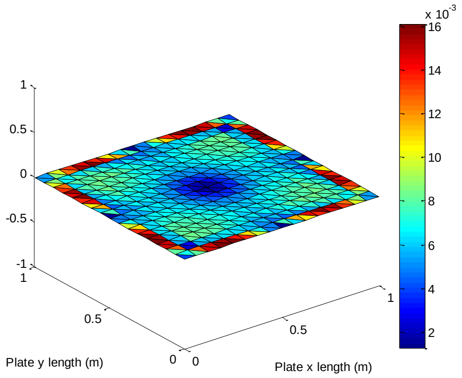
</td><td>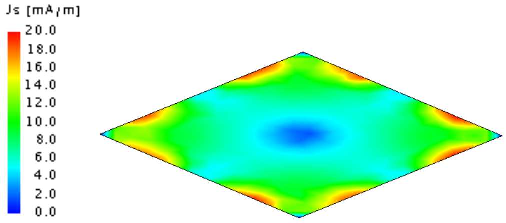
</td></tr>
<tr><td>Maximum surface current on the plate
$J_{max} = 16.0$ [mA/m].</td><td>Maximum surface current on the plate
$J_{max} = 20.0$ [mA/m].</td></tr>
</table>

Figure 24 - The simulation results for dipole with $d = \lambda/10$

<table>
<tr><td colspan="2">Configuration: 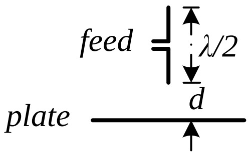
</td></tr>
<tr><td colspan="2">Current distribution on the dipole</td></tr>
<tr><td>Simulation results</td><td>FeKo simulation results</td></tr>
<tr><td>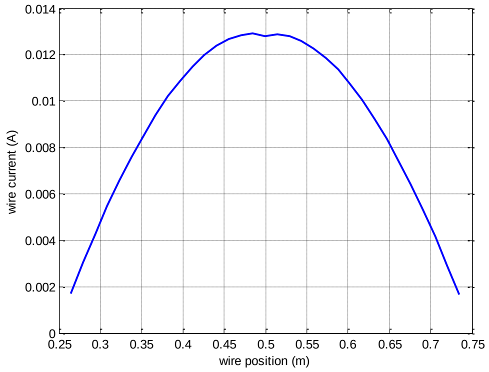
</td><td>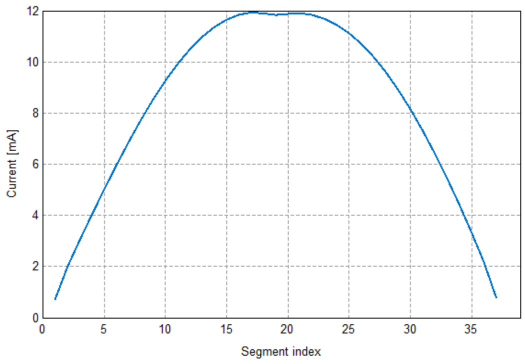
</td></tr>
<tr><td>Maximum current on the wire
$I_{max} = 12.9$ [mA].</td><td>Maximum current on the wire
$I_{max} = 12.0$ m[A].</td></tr>
<tr><td colspan="2">Surface current distribution on the plate</td></tr>
<tr><td>Simulation results</td><td>FeKo simulation results</td></tr>
<tr><td>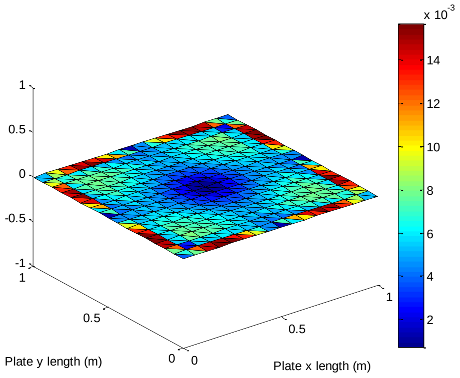
</td><td>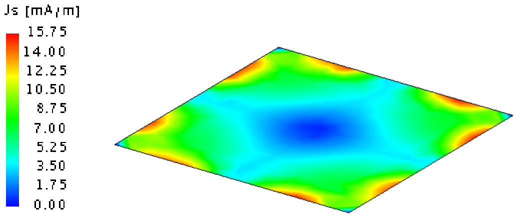
</td></tr>
<tr><td>Maximum surface current on the plate
$J_{max} = 14.5$ [mA/m].</td><td>Maximum surface current on the plate
$J_{max} = 15.7$ [mA/m].</td></tr>
</table>

Figure 25 - The simulation results for dipole with $d = \lambda/4$

Configuration: 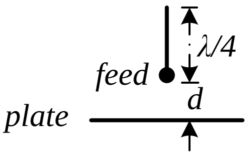	
Current distribution on the quarter wavelength wire	
Simulation results	FeKo simulation results
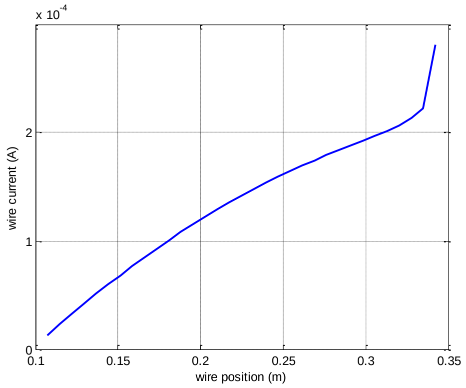	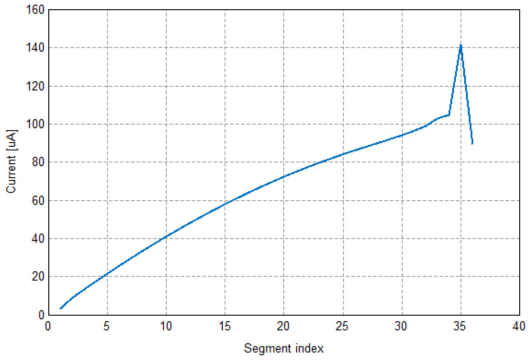
Maximum current on the wire $I_{max} = 0.280$ [mA].	Maximum current on the wire $I_{max} = 0.140$ [mA].
Surface current distribution on the plate	
Simulation results	FeKo simulation results
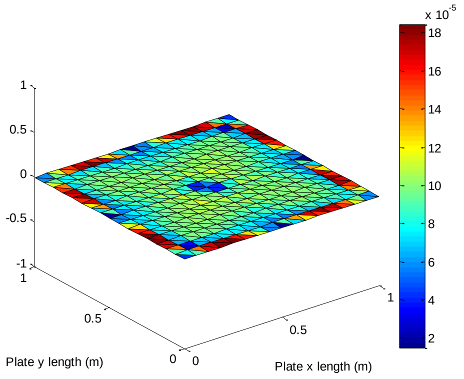	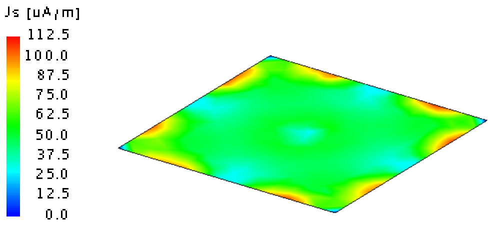
Maximum surface current on the plate $J_{max} = 0.184$ [mA/m].	Maximum surface current on the plate $J_{max} = 0.112$ [mA/m].

Figure 26 - The simulation results for monopole with $d = \lambda/10$

<table>
<tr><td colspan="2">Configuration: 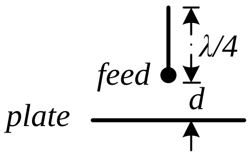
</td></tr>
<tr><td colspan="2">Current distribution on the on the quarter wavelength wire</td></tr>
<tr><td>Simulation results</td><td>FeKo simulation results</td></tr>
<tr><td>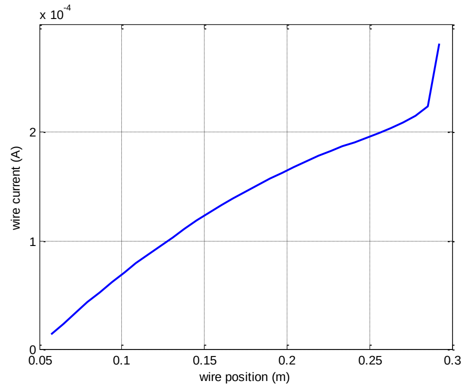
</td><td>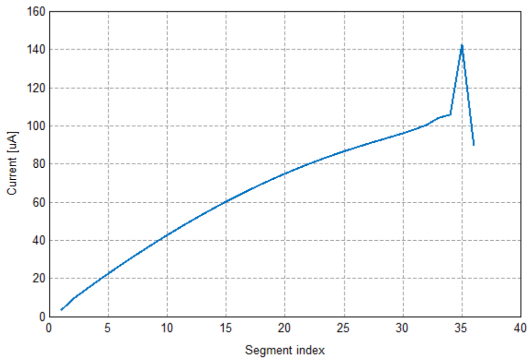
</td></tr>
<tr><td>Maximum current on the wire
$I_{max} = 0.280$ [mA]</td><td>Maximum current on the wire
$I_{max} = 0.140$ [mA]</td></tr>
<tr><td colspan="2">Surface current distribution on the plate</td></tr>
<tr><td>Simulation results</td><td>FeKo simulation results</td></tr>
<tr><td>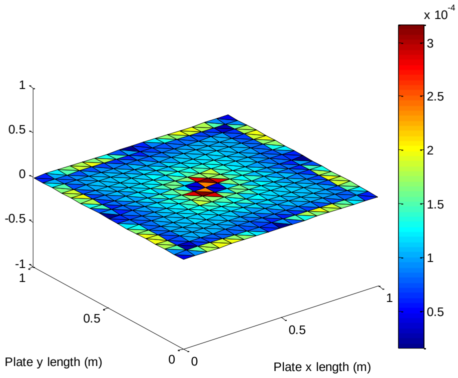
</td><td>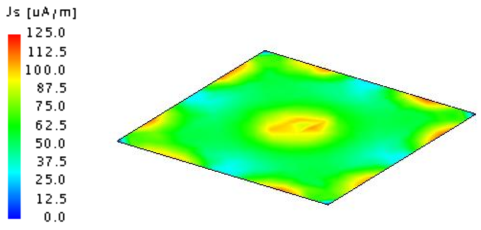
</td></tr>
<tr><td>Maximum surface current on the plate
$J_{max} = 0.316$ [mA/m]</td><td>Maximum surface current on the plate
$J_{max} = 0.125$ [mA/m]</td></tr>
</table>

Figure 27 - The simulation results for monopole with $d = \lambda/20$

During the simulations with FeKo, the source is positioned using the wire port feature of FeKo. This port allows the user to set the source to a position on the wire, but it is not possible to position this port to an edge vertex. FeKo positions the source in such cases to the end segment. Therefore, although the results obtained for the quarter-wavelength wire, which are shown in Figure 26 and Figure 27, are similar in terms of behavior, they differ in terms of current magnitude. This discrepancy may be due to the differences in modeling the excitation.

The simulation results of the developed code and FeKo are found to be in good agreement with the mesh sizes used to simulate: MatLab simulations with 512 triangles on the plate and 35 segments on the wire, and FeKo simulations with 398 segments on the plate and 37 segments on the wire.

In [16], the variation of the input impedance of a half wavelength dipole antenna with the distance *d* is given. In order to compare the results of the developed code, a similar graph is obtained. The imaginary part of the input impedance is found to be quite different from the results given in [16]. But the results for the real part of the input impedance were in good agreement and they are presented in Figure 28.

Generally, a better agreement in the real part of the input impedance is expected compared to the imaginary part. Because, the real part is related to the radiated field, which is less sensitive to the errors in the current distribution due to its stationary nature. On the other hand, the imaginary part is related to the stored energy in the near field of the antenna. So, it is very sensitive to the errors in the current distribution.

Recall that for the wire analysis, staircase approximation shown in Figure 18 is used for handling the singularity problem, but this method results in inaccurate results when the imaginary part of the input impedance is considered.

Input impedance R_{in}	Input impedance of a $\lambda/2$ dipole over a ground plane [16]
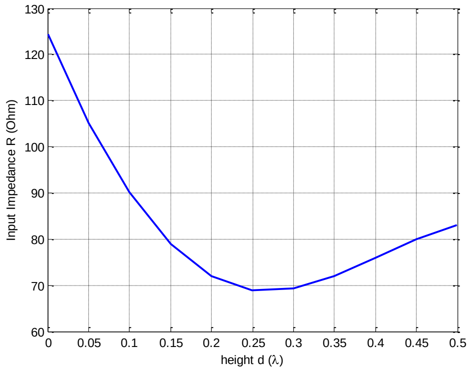	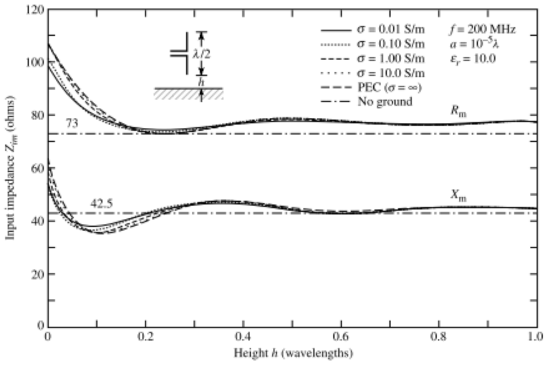

Figure 28 - Input impedance of the dipole over the plate

CHAPTER 6

MOM ANALYSIS OF CONTACTING SURFACE/WIRE STRUCTURES

In order to analyze the current distribution on the surfaces which are connected to wires, a special basis function, also called the "attachment mode", should be defined at the junction to model the current flow from the wire to the plate or vice-versa.

In [4], an attachment mode with triangular basis functions, as shown in Figure 29, is defined that is compatible with RWG basis functions on the plate and triangular basis functions on the wire.

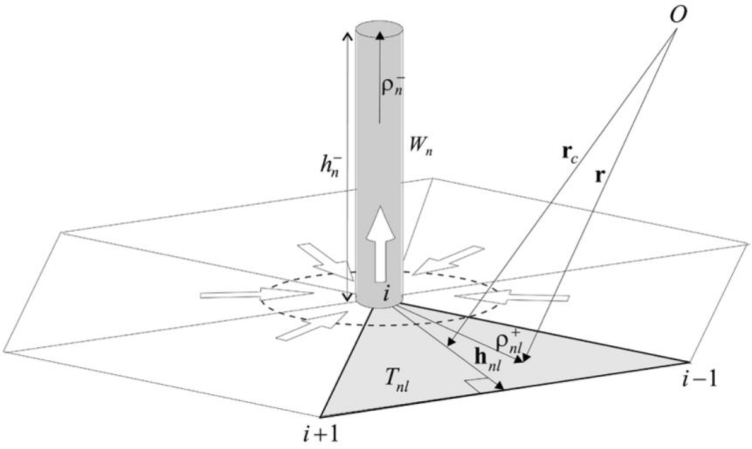

Figure 29 - Representation of junction basis function of triangular basis [3]

The junction basis functions $f_n^a(\boldsymbol{r})$ for the attachment mode are defined as:

$$f_n^a(\boldsymbol{r}) = \begin{cases} K_{nl}\left[1 - \frac{\left(h_{nl}^+\right)^2}{\left(\boldsymbol{\rho}_{nl}^+ \cdot \hat{\boldsymbol{h}}_{nl}^+\right)^2}\right] \frac{\boldsymbol{\rho}_{nl}^+}{h_{nl}^+}, & \boldsymbol{r}\ in\ T_{nl} \\ \frac{\boldsymbol{\rho}_n^-}{h_{nl}^-}, & \boldsymbol{r}\ in\ W_n \\ 0, otherwise & \end{cases} \tag{6.1}$$

where, T_{nl} is l-th triangle of the n-th junction and W_n is the attached wire to the n-th junction. $\boldsymbol{\rho}_{nl}^+$ is the distance vector from the junction vertex to the points on the lth junction triangle and h_{nl}^+ is the vector height of this triangle associated with the edge opposite the junction vertex. $\boldsymbol{\rho}_{\boldsymbol{n}}^-$ is the distance vector from the junction segment points to the free segment node (i.e. $\boldsymbol{\rho}_{\boldsymbol{n}}^{-} = (h_{nl}^{-} - z)\boldsymbol{i}_{\boldsymbol{z}}$) and h_{nl}^{-} is the segment length. K_{nl} is a constant that normalizes the total current entering the wire [3].

$$K_{nl} = \frac{\alpha_{nl}}{l_{nl}\sum_{l=1}^{N_{jn}} \alpha_{nl}} = \frac{\alpha_{nl}}{l_{nl}\alpha_{nl}^{t}} \tag{6.2}$$

where α_{nl} is the angle between two edges of T_{nl} common to the nth junction vertex α_{nl}^{t} is the sum of nth junction vertex angles and l_{nl} is the length of the edge opposite to the junction vertex.

In order to use this basis function in the EFIE formulation, also the divergence of the junction basis functions $f_n^a(\boldsymbol{r})$ is required. The divergence of the junction basis functions is given in [17].

$$\nabla \cdot \boldsymbol{f}_n^a(\boldsymbol{r}) = \begin{cases} \frac{2K_{nl}}{h_{nl}^{+}}, & \boldsymbol{r}\ in\ T_{nl} \\ -\frac{1}{h_{nl}^{-}}, & \boldsymbol{r}\ in\ W_n \\ 0, otherwise \end{cases} \tag{6.3}$$

Note that even though the divergence of the attachment mode is finite, the current itself has a singularity of $\frac{1}{\boldsymbol{\rho}}$ as $\boldsymbol{\rho} \rightarrow 0$ (approaching to the junction).

In Figure 30, red circle denotes the junction node and triangles relevant to the attachment mode are denoted by red.

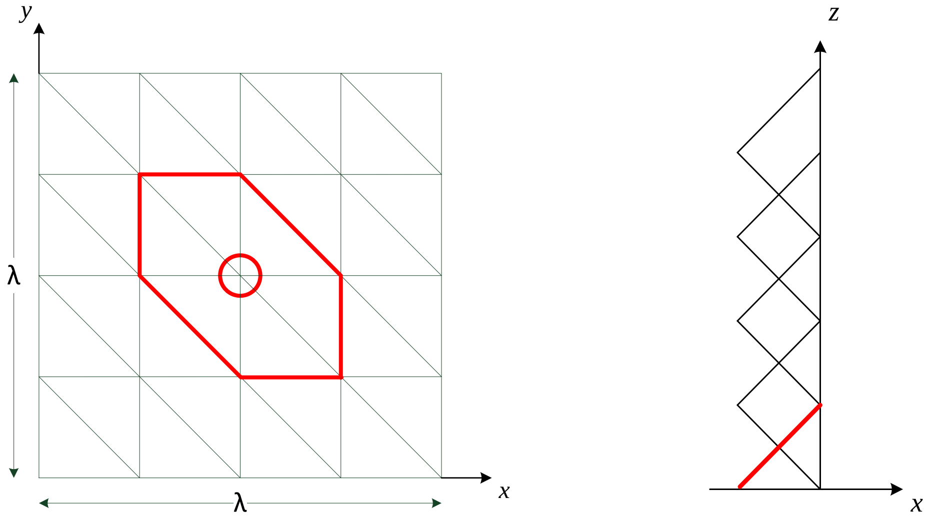

(a) top view (b) side view

Figure 30 - Junction node and attachment mode relevant triangles

3 types of triangles can be identified that are connected to the junction vertex as shown in Figure 31.

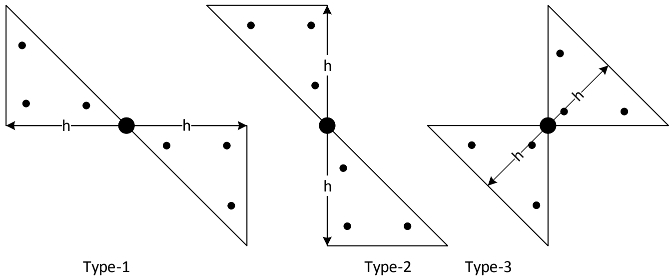

Figure 31 - Triangle types for attachment mode

6.1 METHOD OF MOMENTS FORMULATION

With the use of the attachment mode, an additional unknown is introduced, which is the coefficient of the attachment mode $\boldsymbol{I}_a$. When the attachment mode is considered as well, the MoM matrix discussed in Chapter 5, takes the following form:

$$\boldsymbol{ZI} = \boldsymbol{V} \rightarrow \begin{bmatrix} \boldsymbol{Z}_{PP} & \boldsymbol{C}^{P,W} & \boldsymbol{C}^{P,a} \\ \boldsymbol{C}^{W,P} & \boldsymbol{Z}_{WW} & \boldsymbol{C}^{W,a} \\ \boldsymbol{C}^{a,P} & \boldsymbol{C}^{a,W} & \boldsymbol{Z}_{aa} \end{bmatrix} \cdot \begin{bmatrix} \boldsymbol{I}_P \\ \boldsymbol{I}_W \\ \boldsymbol{I}_a \end{bmatrix} = \begin{bmatrix} \boldsymbol{V}^P \\ \boldsymbol{V}^W \\ \boldsymbol{V}^a \end{bmatrix} \tag{6.4}$$

Since, the overall impedance matrix is a symmetric matrix, $\boldsymbol{C}^{a,P} = [\boldsymbol{C}^{P,a}]^T$ and $\boldsymbol{C}^{a,W} = [\boldsymbol{C}^{W,a}]^T$. Therefore, for the impedance matrix, it is sufficient to calculate additionally the coupling matrices $\boldsymbol{C}^{P,a}$, $\boldsymbol{C}^{W,a}$ and $\boldsymbol{Z}_{aa}$.

6.1.1 CALCULATION OF $\boldsymbol{Z}_{aa}$

The matrix element $\boldsymbol{Z}_{aa}$ is a 1x1 matrix that is obtained by calculating each interaction between triangular segments on the plate and wire segment that are defined for the attachment region. Since the attachment mode is divided into two parts: one on the plate, one on the wire; the self-interaction will consist of 4 terms.

$$j\omega < \boldsymbol{w}_m^a, \boldsymbol{A}(\boldsymbol{r}) >= FactorA_a(I_{a1} + I_{a2} + I_{a3} + I_{a4}) \tag{6.5}$$

where,

$$FactorA_a = \frac{j\omega\mu}{4\pi} \tag{6.6}$$

$$I_{a1} = \int_{T_m} \int_{Tn} \boldsymbol{w}_m^a \cdot \boldsymbol{f}_n^a \frac{e^{-jk|r-r'|}}{|\boldsymbol{r}-\boldsymbol{r}'|} dS_n \, dS_m \tag{6.7}$$

$$I_{a2} = \int_{T_m} \int_{Wn} \boldsymbol{w}_m^a \cdot \boldsymbol{f}_n^a \frac{e^{-jk|r-r'|}}{|\boldsymbol{r}-\boldsymbol{r}'|} dl_n \, dS_m \tag{6.8}$$

$$I_{a3} = \int_{W_m} \int_{Tn} \boldsymbol{w}_m^a \cdot \boldsymbol{f}_n^a \frac{e^{-jk|r-r'|}}{|\boldsymbol{r}-\boldsymbol{r}'|} dS_n \, dl_m \tag{6.9}$$

$$I_{a4} = \int_{W_m} \int_{Wn} \boldsymbol{w}_m^a \cdot \boldsymbol{f}_n^a \frac{e^{-jk|r-r'|}}{|\boldsymbol{r}-\boldsymbol{r}'|} dl_n \, dl_m \tag{6.10}$$

Among these 4 terms, the wire plate interactions for the vector potential contribution of the matrix entries are 0 ($I_{a2} = I_{a3} = 0$) due to the orthogonality of the currents as discussed in Chapter 5. As a result, only the plate-plate and wire-wire interactions should be considered for the vector potential part as follows:

$$I_{a1} = \int_{T_m} \int_{Tn} \left(K_{ml} \left[1 - \frac{\left(h_{ml}^+\right)^2}{\left(\boldsymbol{\rho}_{ml}^+ \cdot \widehat{\boldsymbol{h}}_{ml}^+\right)^2} \right] \frac{\boldsymbol{\rho}_{ml}^+}{h_{ml}^+} \right) \left(K_{nl} \left[1 - \frac{\left(h_{nl}^+\right)^2}{\left(\boldsymbol{\rho}_{nl}^+ \cdot \widehat{\boldsymbol{h}}_{nl}^+\right)^2} \right] \frac{\boldsymbol{\rho}_{nl}^+}{h_{nl}^+} \right) \frac{e^{-jk|r-r'|}}{|\boldsymbol{r}-\boldsymbol{r}'|} dS' \, dS$$

$$= \left(\frac{K_{ml}}{h_{ml}^+} \left[1 - \frac{\left(h_{ml}^+\right)^2}{\left(\boldsymbol{\rho}_{ml}^+ \cdot \widehat{\boldsymbol{h}}_{ml}^+\right)^2} \right] \right) \left(\frac{K_{nl}}{h_{nl}^+} \left[1 - \frac{\left(h_{nl}^+\right)^2}{\left(\boldsymbol{\rho}_{nl}^+ \cdot \widehat{\boldsymbol{h}}_{nl}^+\right)^2} \right] \right) \int_{T_m} \int_{Tn} \boldsymbol{\rho}_{ml}^+ \cdot \boldsymbol{\rho}_{nl}^+ \frac{e^{-jk|r-r'|}}{|\boldsymbol{r}-\boldsymbol{r}'|} dS' \, dS$$

$$I_{a4} = \int_{W_m} \int_{Wn} \left(\frac{\boldsymbol{\rho}_m^-}{h_{ml}^-} \right) \cdot \left(\frac{\boldsymbol{\rho}_n^-}{h_{nl}^-} \right) \frac{e^{-jk|r-r'|}}{|\boldsymbol{r}-\boldsymbol{r}'|} dz' \, dz$$

$$= \left(\frac{1}{h_{ml}^-} \right) \left(\frac{1}{h_{nl}^-} \right) \int_{W_m} \int_{Wn} \boldsymbol{\rho}_{ml}^- \cdot \boldsymbol{\rho}_{nl}^- \frac{e^{-jk|r-r'|}}{|\boldsymbol{r}-\boldsymbol{r}'|} dz' \, dz$$

Similarly the scalar contribution can be written in terms of 4 interactions as:

$$< \boldsymbol{w}_m, \nabla\phi(\boldsymbol{r}) >= FactorPhi_a \left(I_{pa1} + I_{pa2} + I_{pa3} + I_{pa4} \right) \tag{6.11}$$

where,

$$FactorPhi_a = \frac{1}{4\pi\varepsilon j\omega} \tag{6.12}$$

$$I_{pa1} = \int_{T_m} \int_{T_n} (\nabla \cdot \boldsymbol{w}_m)(\nabla \cdot \boldsymbol{f}_n) \frac{e^{-jk|r-r'|}}{|\boldsymbol{r}-\boldsymbol{r}'|} dS' dS \tag{6.13}$$

$$I_{pa2} = \int_{T_m} \int_{W_n} (\nabla \cdot \boldsymbol{w}_m)(\nabla \cdot \boldsymbol{f}_n) \frac{e^{-jk|r-r'|}}{|\boldsymbol{r}-\boldsymbol{r}'|} dz' dS \tag{6.14}$$

$$I_{pa3} = \int_{W_m}\int_{T_n}(\nabla\cdot\boldsymbol{w}_m)(\nabla\cdot\boldsymbol{f}_n)\frac{e^{-jk|r-r'|}}{|\boldsymbol{r}-\boldsymbol{r}'|}dS'dz \tag{6.15}$$

$$I_{pa4} = \int_{W_m}\int_{W_n}(\nabla\cdot\boldsymbol{w}_m)(\nabla\cdot\boldsymbol{f}_n)\frac{e^{-jk|r-r'|}}{|\boldsymbol{r}-\boldsymbol{r}'|}dz'dz \tag{6.16}$$

Substituting the equations for basis and testing functions from equation (6.1) into the integrals above yields:

$$I_{pa1} = \left(\frac{2K_{ml}}{h_{ml}^{+}}\right)\left(\frac{2K_{nl}}{h_{nl}^{+}}\right)\int_{T_m}\int_{T_n}\frac{e^{-jk|r-r'|}}{|\boldsymbol{r}-\boldsymbol{r}'|}dS'dS \tag{6.17}$$

$$I_{pa2} = \left(\frac{2K_{ml}}{h_{ml}^{+}}\right)\left(-\frac{1}{h_{nl}^{-}}\right)\int_{T_m}\int_{W_n}\frac{e^{-jk|r-r'|}}{|\boldsymbol{r}-\boldsymbol{r}'|}dz'dS \tag{6.18}$$

$$I_{pa3} = \left(-\frac{1}{h_{ml}^{-}}\right)\left(\frac{2K_{nl}}{h_{nl}^{+}}\right)\int_{W_m}\int_{T_n}\frac{e^{-jk|r-r'|}}{|\boldsymbol{r}-\boldsymbol{r}'|}dS'dz \tag{6.19}$$

$$I_{pa4} = \left(-\frac{1}{h_{ml}^{-}}\right)\left(-\frac{1}{h_{nl}^{-}}\right)\int_{W_m}\int_{W_n}\frac{e^{-jk|r-r'|}}{|\boldsymbol{r}-\boldsymbol{r}'|}dz'dz \tag{6.20}$$

6.1.2 CALCULATION OF $\boldsymbol{C}^{\boldsymbol{W},\boldsymbol{a}}$

The matrix $\boldsymbol{C}^{W,a}$ is associated with the E-field coupled from the attachment mode to the wire.

$$\boldsymbol{C}^{W,a} = <\boldsymbol{w}_m^W, \boldsymbol{E}^{W,a}> \tag{6.21}$$

Again, the electric field due to the attachment mode will have two components. One for the plate and one for the wire current. The wire-plate interaction will be 0 for the vector potential part. Consequently, the vector potential component will involve only the following wire-attachment (on the wire) interaction.

$$<\boldsymbol{w}_m^a, \boldsymbol{A}(\boldsymbol{r})> = \frac{-j\omega\mu}{4\pi}\int_{W_m}\int_{W^a}\boldsymbol{w}_m^W\cdot f_n^a\frac{e^{-jk|r-r'|}}{|\boldsymbol{r}-\boldsymbol{r}'|}dz'dz \tag{6.22}$$

$$= \frac{-j\omega\mu}{4\pi}\begin{bmatrix}\int_{z_{m-1}}^{z_m}\int_{W^a}\left(\frac{z-z_{m-1}}{z_m-z_{m-1}}\right)\boldsymbol{i_z}\cdot\left(\frac{\boldsymbol{\rho}_{nl}^{-}}{h_{nl}^{-}}\right)\frac{e^{-jk|r-r'|}}{|\boldsymbol{r}-\boldsymbol{r}'|}dz'dz + \\ \int_{z_m}^{z_{m+1}}\int_{W^a}\left(\frac{z_{m+1}-z}{z_{m+1}-z_m}\right)\boldsymbol{i_z}\cdot\left(\frac{\boldsymbol{\rho}_{nl}^{-}}{h_{nl}^{-}}\right)\frac{e^{-jk|r-r'|}}{|\boldsymbol{r}-\boldsymbol{r}'|}dz'dz\end{bmatrix} \tag{6.23}$$

where,

$$\boldsymbol{i_z}\cdot\boldsymbol{\rho}_{nl}^{-} = \boldsymbol{i_z}\cdot(h_{nl}^{-}-z')\boldsymbol{i_z} = (h_{nl}^{-}-z') \tag{6.24}$$

By using (6.24) the vector potential contribution is expressed in the following final form:

$$< \boldsymbol{w}_m^a, \boldsymbol{A}(\boldsymbol{r}) >= \frac{-j\omega\mu}{4\pi}\left[\begin{array}{l} \int_{z_{m-1}}^{z_m}\int_{W^a}\left(\frac{z-z_{m-1}}{z_m-z_{m-1}}\right)\left(\frac{h_{nl}^- - z\prime}{h_{nl}^-}\right)\frac{e^{-jk|r-r'|}}{|\boldsymbol{r}-\boldsymbol{r}'|}dz'dz + \\ \int_{z_m}^{z_{m+1}}\int_{W^a}\left(\frac{z_{m+1}-z}{z_{m+1}-z_m}\right)\left(\frac{h_{nl}^- - z\prime}{h_{nl}^-}\right)\frac{e^{-jk|r-r'|}}{|\boldsymbol{r}-\boldsymbol{r}'|}dz'dz \end{array}\right] \quad (6.25)$$

The scalar potential component of the wire-attachment interaction, consists of 2 parts: first one represents the interaction of the wire currents with the attachment mode on the plate and the second term represents the interaction of the wire currents with the attachment mode on the wire.

$$< \boldsymbol{w}_m^W, \nabla\phi(\boldsymbol{r}) >= FactorPhi_{pwa}\left(I_{pwa1} + I_{pwa2}\right) \quad (6.26)$$

where,

$$FactorPhi_{pwa} = -\frac{1}{4\pi j\omega\varepsilon} \quad (6.27)$$

$$I_{pwa1} = \int_{W_m}\int_{T^a}(\nabla\cdot\boldsymbol{w}_m^W)(\nabla\cdot\boldsymbol{f}_n^a)\frac{e^{-jk|r-r'|}}{|\boldsymbol{r}-\boldsymbol{r}'|}dS'dz \quad (6.28)$$

$$I_{pwa2} = \int_{W_m}\int_{W^a}(\nabla\cdot\boldsymbol{w}_m^W)(\nabla\cdot\boldsymbol{f}_n^a)\frac{e^{-jk|r-r'|}}{|\boldsymbol{r}-\boldsymbol{r}'|}dz'dz \quad (6.29)$$

The explicit expression for the scalar potential contributions are given as

$$I_{pwa1} = I_{pwa11} + I_{pwa12} \quad (6.30)$$

$$I_{pwa2} = I_{pwa21} + I_{pwa22} \quad (6.31)$$

where,

$$I_{pwa11} = \int_{z_{m-1}}^{z_m}\int_{T^a}\left(\frac{1}{z_n-z_{n-1}}\right)\left(\frac{2K_{nl}}{h_{nl}^+}\right)\frac{e^{-jk|r-r'|}}{|\boldsymbol{r}-\boldsymbol{r}'|}dS'dz \quad (6.32)$$

$$I_{pwa12} = \int_{z_m}^{z_{m+1}}\int_{T^a}\left(\frac{-1}{z_{n+1}-z_n}\right)\left(\frac{2K_{nl}}{h_{nl}^+}\right)\frac{e^{-jk|r-r'|}}{|\boldsymbol{r}-\boldsymbol{r}'|}dS'dz \quad (6.33)$$

$$I_{pwa21} = \int_{z_{m-1}}^{z_m}\int_{W^a}\left(\frac{1}{z_n-z_{n-1}}\right)\left(-\frac{1}{h_{nl}^-}\right)\frac{e^{-jk|r-r'|}}{|\boldsymbol{r}-\boldsymbol{r}'|}dz'dz \quad (6.34)$$

$$I_{pwa22} = \int_{z_m}^{z_{m+1}} \int_{W^a} \left(\frac{-1}{z_{n+1}-z_n}\right)\left(-\frac{1}{h_{nl}^{-}}\right)\frac{e^{-jk|r-r'|}}{|\boldsymbol{r}-\boldsymbol{r}'|}\,dz'dz \tag{6.35}$$

6.1.3 CALCULATION OF $\boldsymbol{C}^{\boldsymbol{P},\boldsymbol{a}}$

The matrix $\boldsymbol{C}^{P,a}$ defines the E-field coupled from the attachment to the plate.

$$\boldsymbol{C}^{P,a} =< \boldsymbol{w}_m^P, \boldsymbol{E}^{P,a} > \tag{6.36}$$

For this case in the vector potential component, plate-attachment mode on wire interactions will be 0 and plate-attachment on plate interactions are expressed explicitly as:

$$-j\omega < \boldsymbol{w}_m^P, \boldsymbol{A}(\boldsymbol{r}) >= FactorA_{pa}\left(I_{pa1} + I_{pa2}\right) \tag{6.37}$$

where,

$$FactorA_{pa} = \frac{-j\omega\mu}{4\pi} \tag{6.38}$$

$$I_{pa1} = FactorI_{pa1} \int_{T^+} \int_{T^a} (\boldsymbol{\rho}_m^+ \cdot \boldsymbol{\rho}_{nl}^+)\frac{e^{-jk|\boldsymbol{r}-\boldsymbol{r}'|}}{|\boldsymbol{r}-\boldsymbol{r}'|}\,dS'dS \tag{6.39}$$

with,

$$FactorI_{pa1} = \left(\frac{l_m}{2A_m^+}\right)\left(\frac{K_{nl}}{h_{nl}^+}\left[1 - \frac{\left(h_{nl}^+\right)^2}{\left(\boldsymbol{\rho}_{nl}^+ \cdot \hat{\boldsymbol{h}}_{nl}^+\right)^2}\right]\right) \tag{6.40}$$

$$I_{pa2} = FactorI_{pa2} \int_{T^-} \int_{T^a} (\boldsymbol{\rho}_m^- \cdot \boldsymbol{\rho}_{nl}^+)\frac{e^{-jk|\boldsymbol{r}-\boldsymbol{r}'|}}{|\boldsymbol{r}-\boldsymbol{r}'|}\,dS'dS \tag{6.41}$$

With,

$$FactorI_{pa2} = \left(\frac{l_m}{2A_m^-}\right)\left(\frac{K_{nl}}{h_{nl}^+}\left[1 - \frac{\left(h_{nl}^+\right)^2}{\left(\boldsymbol{\rho}_{nl}^+ \cdot \hat{\boldsymbol{h}}_{nl}^+\right)^2}\right]\right) \tag{6.42}$$

The integrals I_{pa1} and I_{pa2} must be evaluated numerically. Therefore, the integrals that have triangular domain can be written using Gaussian quadrature of order 2. In order to avoid singularity, the observation triangle can be written using Gaussian quadrature of order 1.

The scalar potential component of the plate-attachment interaction involves the following 4 contributions:

$$< \boldsymbol{w}_m^P, \nabla\phi(\boldsymbol{r}) >= FactorPhi_{pa}\left(I_{ppa1} + I_{ppa2} + I_{ppa3} + I_{ppa4}\right) \quad (6.43)$$

where,

$$FactorPhi_{pa} = -\frac{1}{4\pi j\omega\varepsilon} \quad (6.44)$$

$$I_{ppa1} = FactorI_{phi1} \int_{T^+} \int_{T^a} \frac{e^{-jk|r-r'|}}{|\boldsymbol{r}-\boldsymbol{r}'|} dS' dS \quad (6.45)$$

with,

$$FactorI_{ppa1} = \left(\frac{l_m}{A_m^+}\right)\left(\frac{2K_{nl}}{h_{nl}^+}\right) \quad (6.46)$$

$$I_{ppa2} = FactorI_{ppa2} \int_{T^+} \int_{W^a} \frac{e^{-jk|r-r'|}}{|\boldsymbol{r}-\boldsymbol{r}'|} dz' dS \quad (6.47)$$

with,

$$FactorI_{ppa2} = \left(\frac{l_m}{A_m^+}\right)\left(-\frac{1}{h_{nl}^-}\right) \quad (6.48)$$

$$I_{ppa3} = FactorI_{ppa3} \int_{T^-} \int_{T^a} \frac{e^{-jk|r-r'|}}{|\boldsymbol{r}-\boldsymbol{r}'|} dS' dS \quad (6.49)$$

with,

$$FactorI_{ppa3} = \left(-\frac{l_m}{A_m^-}\right)\left(\frac{2K_{nl}}{h_{nl}^+}\right) \quad (6.50)$$

$$I_{ppa4} = FactorI_{ppa4} \int_{T^-} \int_{W^a} \frac{e^{-jk|r-r'|}}{|\boldsymbol{r}-\boldsymbol{r}'|} dz' dS \quad (6.51)$$

with,

$$FactorI_{ppa4} = \left(-\frac{l_m}{A_m^-}\right)\left(-\frac{1}{h_{nl}^-}\right) \quad (6.52)$$

6.2 SIMULATION RESULTS

In the first case, a thin wire of length ${}^{\lambda}/_{4}$ is attached to a plate of size $\lambda \times \lambda$ and the wire is fed from the top. For the structures in this chapter, two different excitation models are studied. First one is the delta gap excitation of 1V considered so far and the other one is the current injection model at the feed point. The injected current is assumed to be a half triangular shape with 1A magnitude at the feed point.

<table>
<tr><td colspan="2">Delta gap excitation (${}^{\lambda}/_{4}$ thin wire)</td></tr>
<tr><td colspan="2">Configuration: 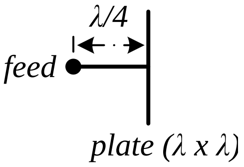 </td></tr>
<tr><td>Current distribution on the wire</td><td>Current distribution on the wire (FeKo)</td></tr>
<tr><td>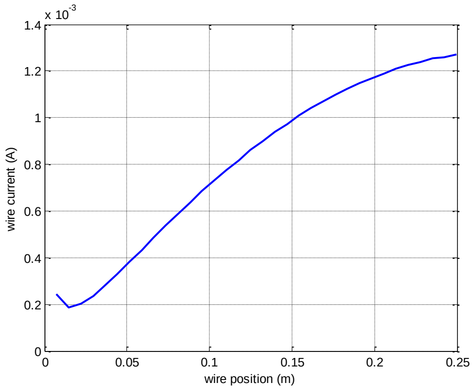 </td><td>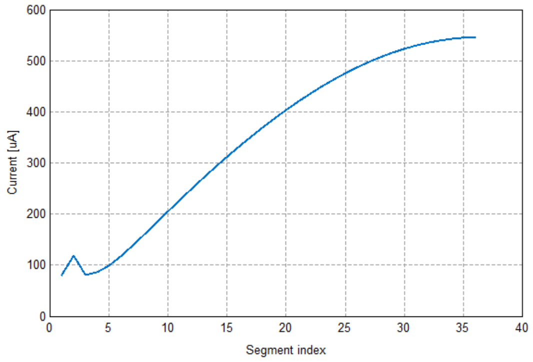 </td></tr>
<tr><td>Maximum current on the wire
$I_{max} = 1.30$ [mA]</td><td>Maximum current on the wire
$J_{max} = 0.545$ [mA]</td></tr>
<tr><td>Current distribution on the plate</td><td>Current distribution on the plate</td></tr>
<tr><td>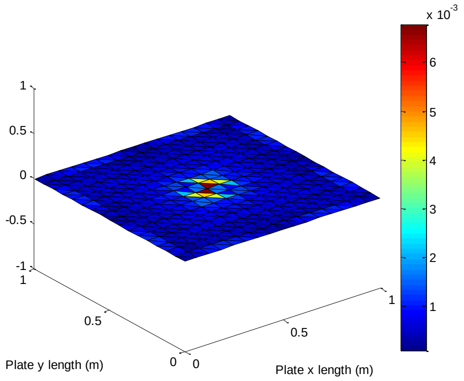 </td><td>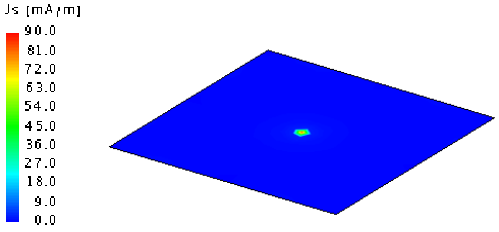 </td></tr>
<tr><td>Maximum current on the plate
$J_{max} = 0.0068$ [A/m]</td><td>Maximum current on the plate
$J_{max} = 0.090$ [A/m]</td></tr>
</table>

Figure 32 - Current distribution on the $\lambda/4$ wire and plate in contacting configuration (delta gap)

<table>
<tr><td colspan="2">Half triangle excitation ($^{\lambda}/_{4}$ thin wire)</td></tr>
<tr><td colspan="2">Configuration: 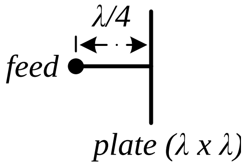
</td></tr>
<tr><td>Current distribution on the wire</td><td>Current distribution on the plate</td></tr>
<tr><td>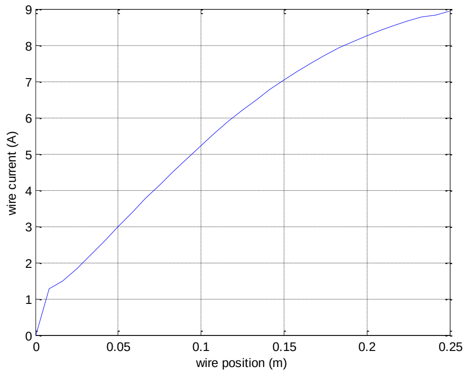
</td><td>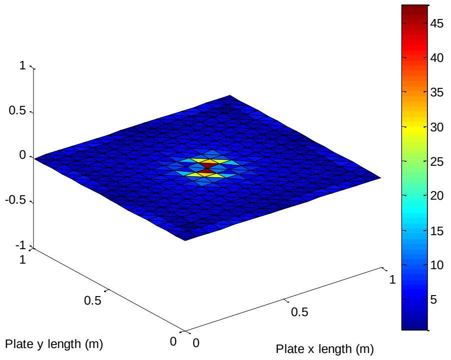
</td></tr>
<tr><td>Maximum current on the wire
$I_{max} = 8.95$ [A]</td><td>Maximum current on the plate
$J_{max} = 47.63$ [A/m]</td></tr>
</table>

Figure 33 - Current distribution on the $\lambda/4$ wire and plate in contacting configuration (triangle excitation)

Here, it is observed that with the junction to the PEC plate, the current distribution on the quarter wavelength thin wire is maximum at the junction point. In the second case, a thin wire of length $\frac{\lambda}{2}$ is attached to a plate of size $\lambda \times \lambda$ is simulated with delta gap excitation of 1V and with a half triangle from the upper end point.

<table>
<tr><td colspan="2">Delta gap excitation ($^{\lambda}/_{2}$ thin wire)</td></tr>
<tr><td colspan="2">Configuration: 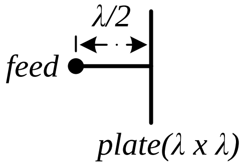
</td></tr>
<tr><td>Current distribution on the wire</td><td>Current distribution on the wire (FeKo)</td></tr>
<tr><td>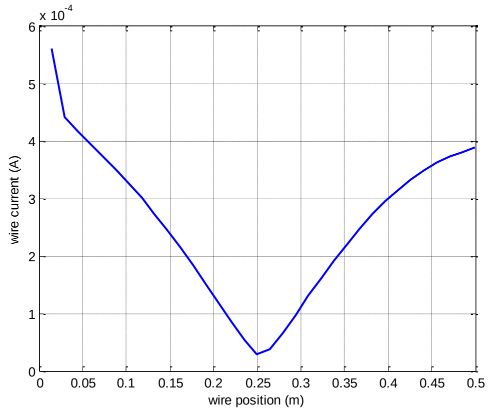
</td><td>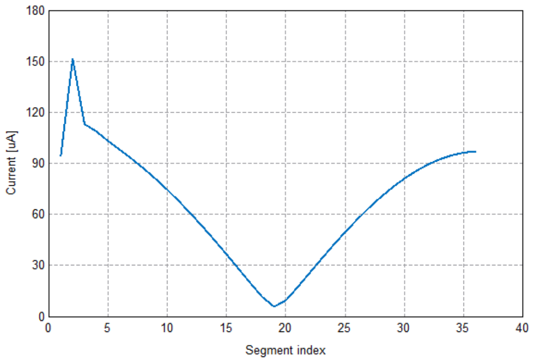
</td></tr>
<tr><td>Current on the wire-plate junction</td><td>Current on the wire-plate junction</td></tr>
</table>

<table>
<tr><td>$I_{max} = 0.499$ [mA]</td><td>$I_{max} = 0.092$ [mA]</td></tr>
<tr><td>Current distribution on the plate</td><td>Current distribution on the plate (FeKo)</td></tr>
<tr><td>
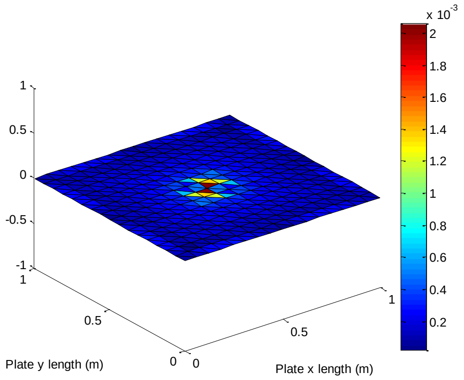

</td><td>
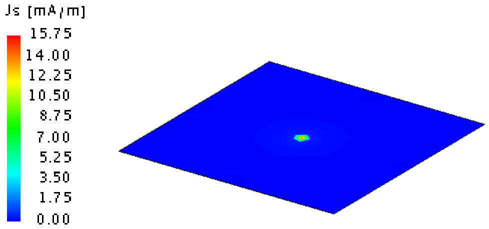

</td></tr>
<tr><td>Maximum current on the plate
$J_{max} = 2.00$ [mA/m]</td><td>Maximum current on the plate
$J_{max} = 15.75$ [mA/m]</td></tr>
</table>

Figure 34 - Current distribution on the $\lambda/2$ wire and plate in contacting configuration (delta gap)

<table>
<tr><td colspan="2">Half triangle excitation ($\lambda/_2$ thin wire)</td></tr>
<tr><td colspan="2">Configuration:
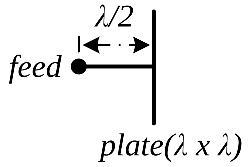

</td></tr>
<tr><td>Current distribution on the wire</td><td>Current distribution on the plate</td></tr>
<tr><td>
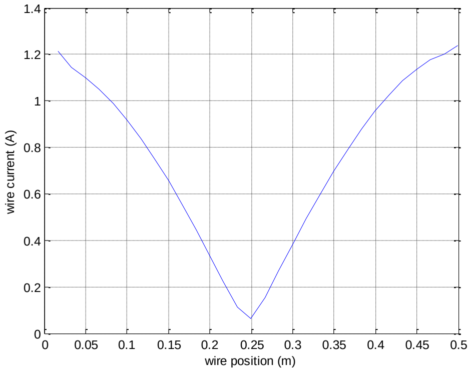

</td><td>
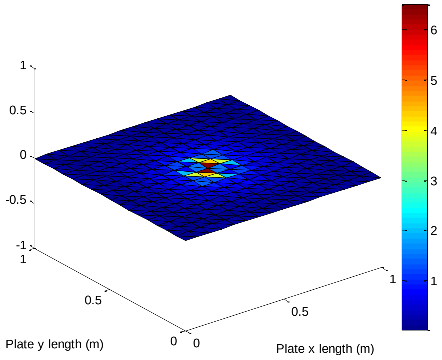

</td></tr>
<tr><td>Current on the wire-plate junction
$I_{max} = 1.24$ [A]</td><td>Maximum current on the plate
$J_{max} = 6.51$ [A/m]</td></tr>
</table>

Figure 35 - Current distribution on the $\lambda/2$ wire and plate in contacting configuration (triangle excitation)

In Figure 34 and Figure 35, it is observed that; when the length of the wire is set to half-wavelength, due to the short-circuit at the junction; the current maximum is obtained at the junction. Due to the image theory, the structure behaves like a half-wavelength dipole with its feed at the junction. Therefore, the current minimum is obtained at $\lambda/4$ distance to the junction. Then, the current rises towards the feed.

Also, when the half-wavelength wire is fed from its mid-point, it is observed that the current at its open load side drops to 0, whereas at its short circuit side (at the junction) reaches maximum. The obtained results are shown in Figure 36.

<table>
<tr><td colspan="2">Delta gap excitation ($^{\lambda}/_{2}$ thin wire)</td></tr>
<tr><td colspan="2">Configuration: 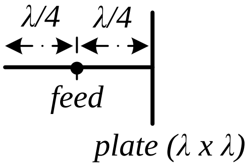
</td></tr>
<tr><td>Current distribution on the wire</td><td>Current distribution on the wire (FeKo)</td></tr>
<tr><td>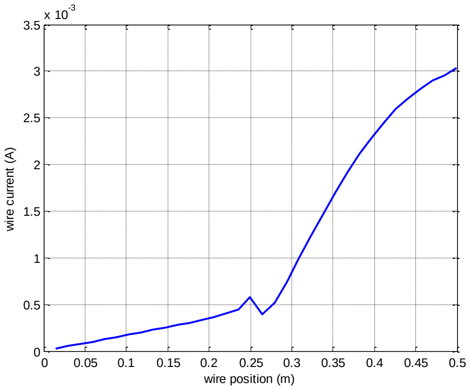
</td><td>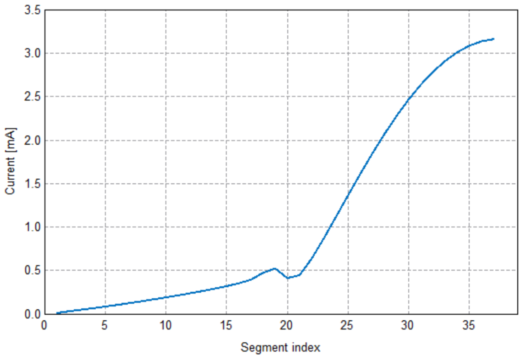
</td></tr>
<tr><td>Maximum current on the wire
$I_{max} = 3.03$ [mA]</td><td>Maximum current on the wire
$J_{max} = 3.16$ [mA]</td></tr>
<tr><td>Current distribution on the plate</td><td>Current distribution on the plate</td></tr>
<tr><td>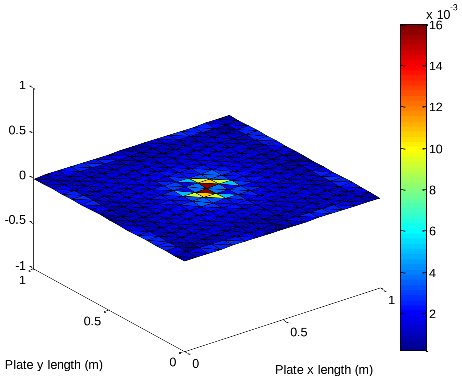
</td><td>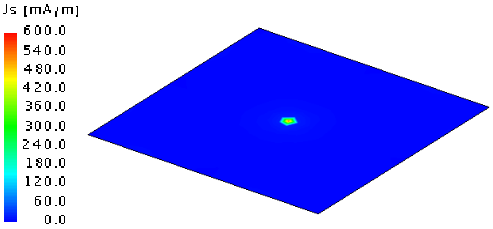
</td></tr>
<tr><td>Maximum current on the plate
$J_{max} = 0.016$ [A/m].</td><td>Maximum current on the plate
$J_{max} = 0.600$ [A/m].</td></tr>
</table>

Figure 36 - Current distribution on the λ/2 wire and plate in contacting configuration (feed at midpoint)

Next, a top loaded monopole structure is examined and compared with the results that are obtained in [18]. In Figure 37, the cross sectional view of a disk loaded monopole antenna is shown.

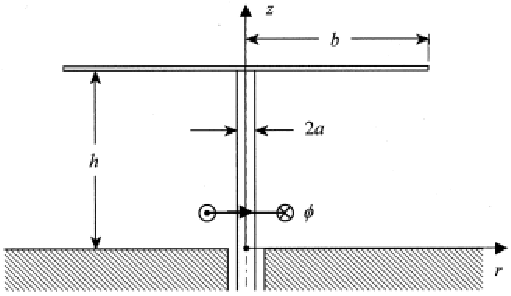

Figure 37 - Top loaded monopole [18]

In our configuration, instead of a disk that is attached to the top of the monopole, a square plate of size given in [18] ($b = 38.7mm$) and a monopole of size given in [18] ($h = 31.75mm,\ and\ a = 1.19mm$) is used. The current distribution on the wire is obtained for given frequencies in [18] and drawn with respect to position. Note that, in [18] the currents are obtained using a magnetic frill generator. Therefore, the units on the current axis are different in Figure 38.

Configuration:	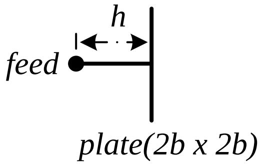
Current distribution on the wire	Current distribution on the wire [18]
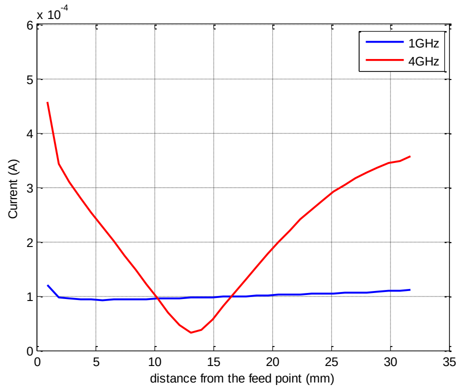	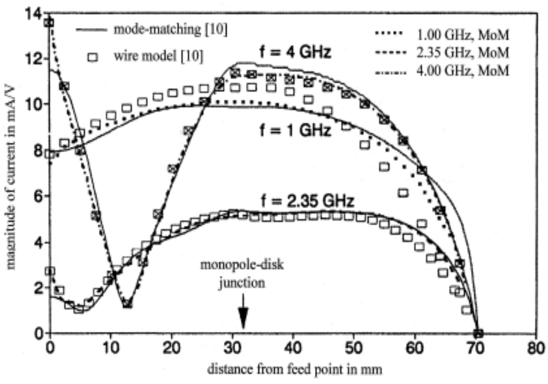

Figure 38 - Current distribution on the top loaded monopole with respect to frequency

When the frequency is 4GHz, the length of the wire corresponds to 0.42λ. Therefore, a similar behavior as in Figure 34 is observed in the Figure 38; the current approaches its minimum at approx. $\lambda/4$ distance from the junction. At 1GHz, the length of the wire corresponds to 0.1λ. Therefore, a current rise towards the junction is observed. The current distribution at 2.35GHz is not included in the graph because of high discrepancy in the magnitude of the results.

<table>
<tr><th colspan="2">Delta gap excitation at several frequencies</th></tr>
<tr><th>Input Impedance (real part)</th><th>Input Impedance (real part) [18]</th></tr>
<tr><td>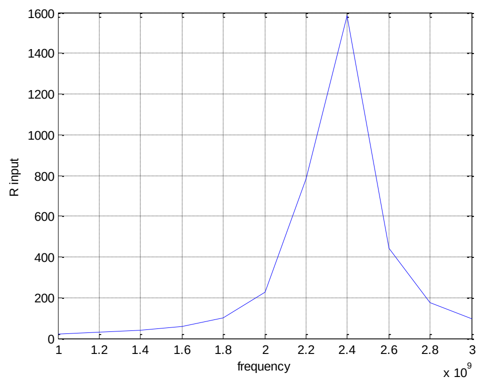
</td><td>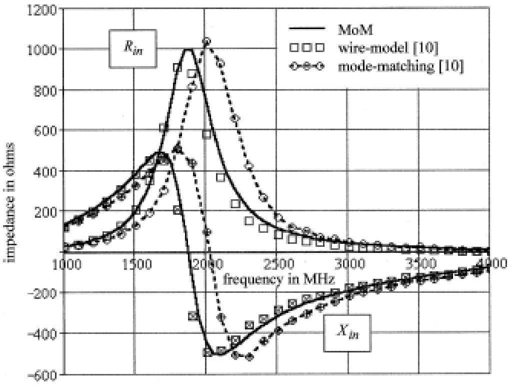
</td></tr>
</table>

Figure 39 - Input impedance of the system in contacting configuration (delta gap)

<table>
<tr><th colspan="2">Half triangle excitation at several frequencies</th></tr>
<tr><th>Input Impedance (real part)</th><th>Input Impedance (real part) [18]</th></tr>
<tr><td>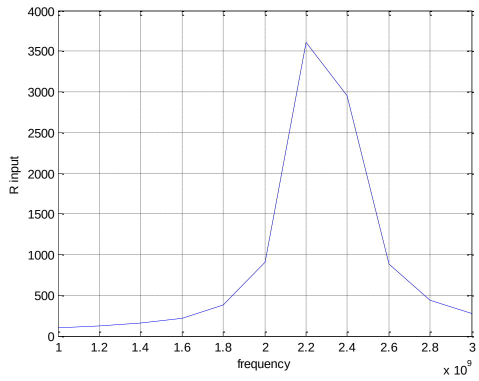
</td><td>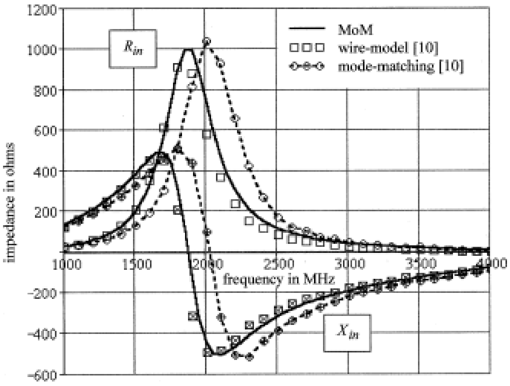
</td></tr>
</table>

Figure 40 - Input impedance of the system in contacting configuration (triangle excitation)

Generally, a better agreement in the real part of the input impedance is expected compared to the imaginary part. Because, the real part is related to the radiated field, which is less sensitive to the errors in the current distribution due to its stationary nature. On the other hand, the imaginary part is related to the stored energy in the near field of the antenna. So, it is very sensitive to the errors in the current distribution.

CHAPTER 7

CONCLUSION AND FUTURE WORK

In this thesis, the method of moments with the Galerkin method and RWG basis functions is used to obtain the surface currents for a PEC square plate. The results are obtained using two singularity handling methods: S.Makarov's method from [6] and Direct Evaluation Method (DEMCEM).

Next, a half wave length dipole is analyzed using MoM and the current distribution of the dipole is obtained.

Afterwards, the coupled current distribution on the dipole and on the plate is simulated together when the dipole is excited with a delta-gap voltage source and is located near the plate and. The same simulation is repeated for a monopole antenna of length $\lambda/_{4}$. The simulation results are compared with FeKo simulation results.

At the end, the formulation for the wire-surface attachment is derived and the attachment mode from [4] that is defined for triangular surfaces and compatible RWG basis functions is described. The total simulation for surface currents of the wire-plate attachment is obtained and compared with FeKo simulation results.

Using this configuration a top loaded monopole antenna is simulated and the results are compared with the results found in [18].

During the simulations, it is seen that, due to inaccurate singularity handling, although the real part of the input impedance, which affects radiation, returned accurate results, the imaginary part contains inaccuracies. So, the inaccurate singularity handling resulted in stored energy part of the antenna.

At simulations for contacting configuration, it is observed that although the behavior of the current distribution matches with the results found in literature and FeKo, the magnitudes are found to be quite different. This problem encountered because of the $1/_{\boldsymbol{\rho}}$ singularity that exists in the basis function of the attachment mode. There are suggested methods in literature [19] to handle this singularity in an accurate way. These methods could not be implemented because of time insufficiency, but they can be part of a future work.

Another issue that might be part of a future work would be the simulation of a probe fed microstrip patch antenna. In order to extend this simulation, instead of free space Green’s function, the layered media Green’s function should be used because of the dielectric environment and using discrete complex image method, the simulation can be extended to simulate a probe fed microstrip patch antenna.

REFERENCES

[1] R.F.Harrington, "*Field Computation by Moment Method",* MacMillan, New York, 1968

[2] S.M.Rao, D.R.Wilton and A.W.Glisson, "Electromagnetic Scattering by Surfaces of Arbitrary Shape", *IEEE Transactions on Antennas and Propagation,* vol. AP-30, no. 3, pp. 409-418, May 1982

[3] J.M.Taboada, "Evaluation of Galerkin Integrals Involving Triangular-Type Wire-to-Surface Junctions in the Method of Moments", *IEEE Transactions on Antennas and Propagation,* vol. 52, no. 10, pp. 2785-2789, Oct 2004

[4] S.U.Hwu, D.R.Wilton and S.M.Rao, "Electromagnetic Scattering and Radiation by Arbitrary Conducting Wire/Surface Configurations", *in Proc. IEEE Int. Antennas and Propagat. Symp.,* vol. 26, pp. 890–893, June 1988

[5] J.C.G.Matthews and G.G.Cook, "An Efficient Method for Attaching Thin Wire Monopoles to Surfaces Modeled Using Triangular Patch Segmentation", *IEEE Transactions on Antennas and Propagation,* vol. 51, no. 7, pp. 1623-1629, July 2003

[6] S.N.Makarov, "*Antenna and EM Modeling with MATLAB",* John Wiley and Sons, Inc., 2002

[7] A.G.Polimeridis and J.R.Mosig, "On the Direct Evaluation of Surface Integral Equation Impedance Matrix Elements Involving Point Singularities", *IEEE Antennas and Wireless Propagation Letters*, vol. 10, pp. 509-602, 2011

[8] J.-M.Jin, "*Theory and Computation of Electromagnetic Fields",* John Wiley and Sons, Inc., 2010

[9] W.C.Gibson, "*The Method of Moments in Electromagnetics",* Chapman & Hall/CRC, 2008

[10] D.A.Dunavant, "High degree efficient symmetrical Gaussian quadrature rules for the triangle", *Int. J. Num. Meth. Eng.*, vol. 21, pp. 1129–1148, 1985

[11] S.Järvenpää, M.Taskinen, and P.Ylä-Oijala, “Singularity Subtraction Technique for High-Order Polynomial Vector Basis Functions on Planar Triangles”, *IEEE Transactions on Antennas and Propagation,* vol. 54, no. 1, pp. 42-49, Jan 2006

[12] M.A.Khayat and D.R.Wilton, “Numerical Evaluation of Singular and Near-Singular Potential Integrals”, *IEEE Transactions on Antennas and Propagation*, vol. 53, no. 10, pp. 3180-3190, October 2005

[13] M.G.Duffy, “Quadrature over a pyramid or cube of integrands with a singularity at a vertex”, SIAM J. Num. Anal., vol.19, no.6, pp. 1260-1262, 1982

[14] A.G.Polimeridis, I.D.Kouffogiannis, M.Mattes and J.R.Mosig, “Considerations on Double Exponential-Based Cubatures for the Computation of Weakly Singular Galerkin Inner Products” IEEE Transactions on Antennas and Propagation, vol. 60, no. 5, pp. 2579-2582, May 2012

[15] A.G.Polimeridis, “DEMCEM: a Matlab/C++ package for the computation of singular integrals arising in Galerkin EM SIE formulations” [pdf] Available at: http://web.mit.edu/thanos_p/www/ReadMe_DEMCEM.pdf

[16] C.A.Balanis, “*Antenna Theory Analysis and Design”,* John Wiley & Sons, Inc., New Jersey, 2005

[17] N.J.Champagne, W.A.Johnson and D.R.Wilton, “On Attaching a Wire to a Triangulated Surface”, *Institute of Electrical and Electronics Engineers Antennas and Propagation Society Symposium*, San Antonio, TX, June 16-21, 2002

[18] T.L.Simpson, “The Disk Loaded Monopole Antenna”, *IEEE Transactions on Antennas and Propagation*, vol.52, no.2, pp. 542-550, February 2004

[19] F.Vipiana, “Optimized Numerical Evaluation of Singular and Near-Singular Potential Integrals Involving Junction Basis Functions”, *IEEE Transactions on Antennas and Propagation*, vol. 59, no. 1, pp. 162-171, January 2011

[20] C.Marasini, *“Efficient computation techniques for Galerkin MoM antenna design”,* Ph.D. Dissertation, Technische Universiteit Eindhoven, 2008.

[21] D.J.Taylor, *Evaluation of Singular Electric Field Integral Equation (EFIE) Matrix Elements,* Naval Research Laboratory Washington, June 2001

[22] T.-I.Suh, S.-S.Lee, and H.-T.Kim, “Mutual Coupling Reduction of Antennas on A Complex Superstructure”, *Journal of Electromagn. Waves and Appl.*, vol. 18, no. 7, pp. 983–991, 2004

[23] A.G.Polimeridis and T.V.Yioultsis, “On the Direct Evaluation of Weakly Singular Integrals in Galerkin Mixed Potential Integral Equation Formulations”, *IEEE Transactions on Antennas and Propagation,* vol. 56, no. 9, pp. 3011-3019, Sept 2008

[24] L.J.Gray, A.Salvadori, A.-V. Phan and V.Mantic, “Direct Evaluation of Hypersingular Galerkin Surface Integrals. II”, *Electronic Journal of Boundary Elements*, vol. 4, no. 3, pp. 105-130, 2006

APPENDIX

The ready to use MatLab library for DEMCEM, calculates the MoM matrix entries for coinciding triangles. As shown in Figure 41, since 3 different RWG pairs share the same triangle T#1, there occurs a singularity whenever a calculation between these 3 RWG pairs is required. Assuming that T#3 and T#1 have the basis function f_1 , T#1 and T#2 have the basis f_2 and T#4 and T#1 have the basis function f_3.

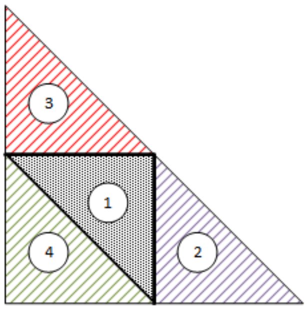

Figure 41 - RWG pairs sharing a triangle

The outputs of the DEMCEM library is a vector of 9 elements and denoted by$I_DE(n)|_{n=1}^{9}$. By using this output vector, the matrix entries can be calculated as:

$$Z_{11} = < f_1, \mathcal{L}(f_1) >= \frac{\sqrt{\frac{\mu}{\varepsilon}}}{4\pi} I\_DE(1) \cdot sign_{RWG\#1}(T\#1) \cdot sign_{RWG\#1}(T\#1)$$

$$Z_{12} = < f_1, \mathcal{L}(f_2) >= \frac{\sqrt{\frac{\mu}{\varepsilon}}}{4\pi} I\_DE(2) \cdot sign_{RWG\#1}(T\#1) \cdot sign_{RWG\#2}(T\#1)$$

$$Z_{13} = < f_1, \mathcal{L}(f_3) >= \frac{\sqrt{\frac{\mu}{\varepsilon}}}{4\pi} I\_DE(3) \cdot sign_{RWG\#1}(T\#1) \cdot sign_{RWG\#3}(T\#1)$$

$$Z_{21} = < f_2, \mathcal{L}(f_1) >= \frac{\sqrt{\frac{\mu}{\varepsilon}}}{4\pi} I\_DE(4) \cdot sign_{RWG\#2}(T\#1) \cdot sign_{RWG\#1}(T\#1)$$

$$Z_{22} = < f_2, \mathcal{L}(f_2) >= \frac{\sqrt{\frac{\mu}{\varepsilon}}}{4\pi} I\_DE(5) \cdot sign_{RWG\#2}(T\#1) \cdot sign_{RWG\#2}(T\#1)$$

$$Z_{23} = < f_2, \mathcal{L}(f_3) >= \frac{\sqrt{\frac{\mu}{\varepsilon}}}{4\pi} I\_DE(6) \cdot sign_{RWG\#2}(T\#1) \cdot sign_{RWG\#3}(T\#1)$$

$$Z_{31} = < f_3, \mathcal{L}(f_1) >= \frac{\sqrt{\frac{\mu}{\varepsilon}}}{4\pi} I\_DE(7) \cdot sign_{RWG\#3}(T\#1) \cdot sign_{RWG\#1}(T\#1)$$

$$Z_{32} = < f_3, \mathcal{L}(f_2) >= \frac{\sqrt{\frac{\mu}{\varepsilon}}}{4\pi} I\_DE(8) \cdot sign_{RWG\#3}(T\#1) \cdot sign_{RWG\#2}(T\#1)$$

$$Z_{33} = < f_3, \mathcal{L}(f_3) >= \frac{\sqrt{\frac{\mu}{\varepsilon}}}{4\pi} I\_DE(9) \cdot sign_{RWG\#3}(T\#1) \cdot sign_{RWG\#3}(T\#1)$$